# THE REFLECTANCE OF HUMAN SKIN IN THE EXTENDED INFRARED REGION USING A FABRY-PEROT BASED SPECTRAL MEASUREMENT TECHNIQUE

A THESIS SUBMITTED TO
THE GRADUATE SCHOOL OF NATURAL AND APPLIED SCIENCES
OF
MIDDLE EAST TECHNICAL UNIVERSITY

BY

MERVE KILIÇ DİNÇER

IN PARTIAL FULFILLMENT OF THE REQUIREMENTS
FOR
THE DEGREE OF MASTER OF SCIENCE
IN
PHYSICS

SEPTEMBER 2023

Approval of the thesis:

**THESIS TITLE**

submitted by **MERVE KILIÇ DİNÇER** in partial fulfillment of the requirements for the degree of **Master of Science** i**n Physics, Middle East Technical University** by,

Prof. Dr. Halil Kalıpçılar
Dean, Graduate School of Natural and Applied Sciences _____

Prof. Dr. Seçkin Kürkçüoğlu
Head of the Department, Physics _____

Assist. Prof. Dr. Hakan Altan
Supervisor, Physics, METU _____

**Examining Committee Members:**

Prof. Dr. Asaf Behzat Şahin
Electrical and Electronics Engineering, Ankara Yıldırım Beyazıt University _____

Prof. Dr. Hakan Altan
Physics, METU _____

Prof. Dr. Okan Esentürk
Chemistry, METU _____

Date: 07.09.2023

**I hereby declare that all information in this document has been obtained and presented in accordance with academic rules and ethical conduct. I also declare that, as required by these rules and conduct, I have fully cited and referenced all material and results that are not original to this work.**

Name Last name : Merve Kılıç Dinçer

Signature :

## ABSTRACT

### THE REFLECTANCE OF HUMAN SKIN IN THE EXTENDED INFRARED REGION USING A FABRY-PEROT BASED SPECTRAL MEASUREMENT TECHNIQUE

Dinçer Kılıç, Merve
Master of Science, Physics
Supervisor : Prof. Dr. Hakan Altan

September 2023, 58 pages

Understanding the optical properties of human skin is important for many current applications. Experimental studies aided by mathematical models will allow important improvements for optical bio-measurement tools. By using a novel Fabry-Perot-based MEMS type tunable wavelength filter we show that precise measurements can be performed in the traditionally hard-to-reach extended near-infrared region. Although there is a large amount of data on the optical properties of human skin in the visible spectral region, there is limited data in the extended infrared region. Of the many studied in the literature the characteristic properties of skin are not well documented in the spectral region above 2000nm due to the higher absorption of water and limitations with instrumentation. Especially for in-vivo measurements, real-time analysis is crucial to better estimate scattering parameters which can shed light on limitations of detection of various species that show resonant features in this spectral region. The approach in our study is based on using a Fabry-Perot-based MEMS type tunable wavelength filter to measure and quantify the scattering parameters of human skin in the extended NIR region. The validity of the obtained parameters is checked by applying a similar measurement scheme in the

1550-1950nm region where multiple studies in the literature have already been performed. Using Monte-Carlo methods based on multi-layer model simulation of human skin the scattered radiation is modeled and the measurement quality is assessed. Due to the limited penetration of ex-NIR light, a 3-layer model is then used for simulating the measurements in the 2000-2450nm region, and scattering and absorption parameters are obtained for each layer. A three-layer model of skin is sufficient for modeling the observed reflectance of ex-NIR light in the 2000-2450nm region. The absorptive and scattering parameters obtained with the results agree well with other published works for wavelengths below 2200nm. This study demonstrates that devices that utilize a MEMS-based rapidly tunable Fabry-Perot-based spectral measurement technique can be applied for in-vivo studies where real-time monitoring is necessary for accurate analysis.

Keywords: Monte Carlo, Skin Reflectance, Human skin, Absorption Coefficient, Scattering Coefficient

# ÖZ

## FABRY-PEROT TABANLI SPEKTRAL ÖLÇÜM TEKNİĞİ İLE GENİŞLETİLMİŞ KIZILÖTESİ BÖLGEDEKİ İNSAN CİLTİNİN YANSIMASI

Dinçer Kılıç, Merve
Yüksek Lisans, Fizik
Tez Yöneticisi: Prof. Dr. Hakan Altan

Eylül 2023, 58 sayfa

İnsan derisinin optik özelliklerini anlamak, birçok güncel uygulama için önemlidir. Matematiksel modellerle desteklenen deneysel çalışmalar, optik biyo-ölçüm araçları için önemli gelişmeler sağlayacaktır. Çalışmamızda yeni bir Fabry-Perot tabanlı MEMS tipi ayarlanabilir dalga boyu filtresi kullanarak, geleneksel olarak ulaşılması zor genişletilmiş yakın kızılötesi bölgede hassas ölçümlerin yapılabileceğini gösteriyoruz. Görünür spektral bölgede insan derisinin optik özellikleri hakkında çok miktarda veri olmasına rağmen, genişletilmiş kızılötesi bölgede sınırlı veri bulunmaktadır. Literatürde incelenen birçok çalışmadan derinin karakteristik özellikleri, esas olarak daha yüksek su emilimi ve enstrümantasyonla ilgili sınırlamalar nedeniyle 2000nm'nin üzerindeki spektral bölgede iyi belgelenmemiştir. Özellikle in-vivo ölçümler için, bu spektral bölgede rezonans özellikler gösteren çeşitli türlerin tespitindeki sınırlamalara ışık tutabilen saçılma parametrelerini daha iyi tahmin etmek için gerçek zamanlı analiz çok önemlidir. Çalışmamızdaki yaklaşım, genişletilmiş NIR bölgesindeki insan derisinin saçılma parametrelerini ölçmek için Fabry-Perot tabanlı MEMS tipi ayarlanabilir dalga boyu filtresi

kullanmaya dayanmaktadır. Elde edilen parametrelerin geçerliliği, literatürde birçok çalışmanın yapıldığı 1550-1950nm bölgesinde benzer bir ölçüm şeması uygulanarak kontrol edilir. İnsan derisinin çok katmanlı model simülasyonuna dayalı Monte-Carlo yöntemleri kullanılarak saçılan radyasyon modellenir ve ölçüm kalitesi değerlendirilir. Ex-NIR ışığının sınırlı penetrasyonu nedeniyle 2000-2450nm bölgesindeki ölçümleri simüle etmek için 3 katmanlı bir model kullanılır ve her katman için saçılma ve absorpsiyon parametreleri elde edilir. Sonuçlarla elde edilen soğurma ve saçılma parametreleri, 2200nm'nin altındaki dalga boyları için yayınlanmış diğer çalışmalarla iyi bir uyum içindedir. Bu çalışma, MEMS tabanlı hızla ayarlanabilen Fabry-Perot tabanlı spektral ölçüm tekniğini kullanan cihazların, doğru analiz için gerçek zamanlı izlemenin gerekli olduğu in-vivo araştırmalar için uygulanabileceğini göstermektedir.

Anahtar Kelimeler: Monte Carlo, Deri Yansıması, İnsan Derisi, Soğurma Katsayısı, Saçılma Katsayısı

Dedication to My Family and My Husband

## ACKNOWLEDGMENTS

I would like to express my deep and sincere gratitude to my research supervisor, Prof. Dr. Hakan Altan, Middle East Technical University, for allowing me to do research and providing invaluable guidance throughout this research. His vision, sincerity, and motivation have deeply inspired me. He has taught me the methodology to carry out the research and to present the research work as clearly as possible. It was a great privilege and honor to work and study under his guidance.

I am extremely grateful to my parents Ali-Vildan Kılıç for their love, caring, and sacrifices for educating and preparing me for my future. I am very thankful to my husband Nart Dinçer for his love, understanding, and continuing support in completing this research work.

Also, I express my thanks to my sister Derya Kılıç and brother Oktay Kılıç for their love and support.

I extend my special thanks to my friends Mehmet Tabak and Yinal Bursa for the keen interest shown in completing this thesis.

## TABLE OF CONTENTS

ABSTRACT ..... v

ÖZ ..... vii

ACKNOWLEDGMENTS ..... x

TABLE OF CONTENTS ..... xi

LIST OF TABLES ..... xiii

LIST OF FIGURES ..... xiv

LIST OF ABBREVIATIONS ..... xvi

1 INTRODUCTION ..... 1

1.1 Human Skin Properties ..... 3

1.1.1 Epidermis ..... 3

1.1.2 Dermis ..... 6

1.1.3 Subcutaneous ..... 7

1.2 Optical Methods for Detection of Glucose, Alcohol, and Blood Parameters Detection: A Background Review ..... 8

1.3 Scope of Thesis ..... 10

2 BACKGROUND ..... 13

2.1 Optical Measurement of Human Skin ..... 13

2.1.1 Absorption ..... 19

2.1.2 Scattering ..... 21

2.2 Monte Carlo Analysis Method ..... 24

3 MEASUREMENTS ..... 27
3.1 Experimental Set-up ..... 27
3.2 Fabry Perot Principles ..... 29
3.3 Measurements ..... 30
4 MONTE CARLO SIMULATIONS ..... 35
4.1 Details of Simulations ..... 35
4.2 1550-1950 nm Region ..... 37
4.3 2000-2450 nm Region ..... 40
5 CONCLUSIONS ..... 47
REFERENCES ..... 49

## LIST OF TABLES

**Table 3.1:** Optical Parameters ..... 28

**Table 4.1:** The skin parameters taken from literature used in the simulation at 1550-1950 nm. The detail of simulations references used are stated in table. ..... 38

**Table 4.2:** Skin Parameters at 2000-2450 nm. The detail of simulations data used are stated in table. While the numbers in red are the data we obtained, black numbers are taken from literature. ..... 43

## LIST OF FIGURES

**Figure 1.1:** Electromagnetic spectrum graph. Adapted from [2]. ..... 1
**Figure 1.2:** The characteristic penetration depth in skin for light from the UV to NIR (1/e). Adapted from [7]..... 2
**Figure 1.3:** Structure of Epidermis. Adapted from [18]**.** ..... 4
**Figure 1.4:** Structure of Dermis. Adapted from [25]**.** ..... 6
**Figure 2.1:**Schematic representation of reflection, absorption, and scattering phenomenon. Adapted from [48]**.** ..... 14
**Figure 2.2:**Structure of Optical Fiber ..... 16
**Figure 2.3:** Schematic representation of the progression of light inside the fiber. Adapted from [50]. ..... 17
**Figure 2.4**: Example of assumption made with a large fiber diameter. ..... 19
**Figure 2.5:** Example of assumption made with many fibers of small diameter. .... 19
**Figure 2.6:**Schematic diagram of absorption on human skin. ..... 20
**Figure 2.7**: Schematic diagram of scattering on human skin. ..... 21
**Figure 3.1:**Thorlabs SLS201L Light Source ..... 27
**Figure 3.2:**The Experimental Setup demonstrates recording measurements taken from the bottom tip of the index finger on an etalon+detector using a Thorlabs model SLS201L broadband light source and then analyzing them on a computer. ..... 28
**Figure 3.3:**Fabry–Perot interferometer. Adapted from [71]. ..... 30
**Figure 3.4:**Measured reflectance data for human skin in the 1550-1950 nm spectral regions. ..... 31
**Figure 3.5**: Comparison of measured reflectance data and published reflectance values in 1550-1950 nm. ..... 32
**Figure 3.6:** Measured reflectance data for human skin in the 2000-2450 nm spectral regions. ..... 32
**Figure 3.7:** Comparison of measured reflectance data and published reflectance values in the 2000-2450 nm. ..... 33

**Figure 4.1**: Schematic structure of three layers of human skin. ..... 37
**Figure 4.2:** Measured and simulated reflectance data for human skin in the 1550-1950 nm spectral regions. Black dots showed the reflectance result of Cooksey and Allen [81], [82], red dots our simulation results, and blue dots our experimental measurements. ..... 38
**Figure 4.3:** Measured and simulated reflectance data for human skin in the 2000-2450nm spectral region. Black dots showed the reflectance result of Cooksey and Allen[81], [82], red dots our optimized simulation results, and blue dots our experimental measurements. ..... 42
**Figure 4.4:** Comparison figure of data taken from literature results, simulation with error bar added and measurement results. ..... 45

## LIST OF ABBREVIATIONS

| | |
|---|---|
| BLL | The Beer-Lambert Law |
| EX-NIR | Extended Near Infrared Region |
| FP | Fabry Perot |
| MC | Monte Carlo |
| MCML | Monte Carlo Multi-Layered |
| NIR | Near Infrared Region |
| NM | Nanometer |
| OPL | Optical Path Length |

# CHAPTER 1

# INTRODUCTION

The optical properties of human skin continue to be of interest to a wide scientific community with models and parameters ever more improving with the development of new tools and methods. The development of non-invasive techniques to monitor and even in some cases diagnose people is inherently tied to optical measurements. With the development of new light sources and detecting techniques a wide range of studies are being implemented to understand the properties of human skin and with that understand the measurement capability that can be achieved. Ultrasound imaging, x-ray radiography, x-ray computed tomography, and magnetic resonance imaging are the most common medical imaging modalities [1].

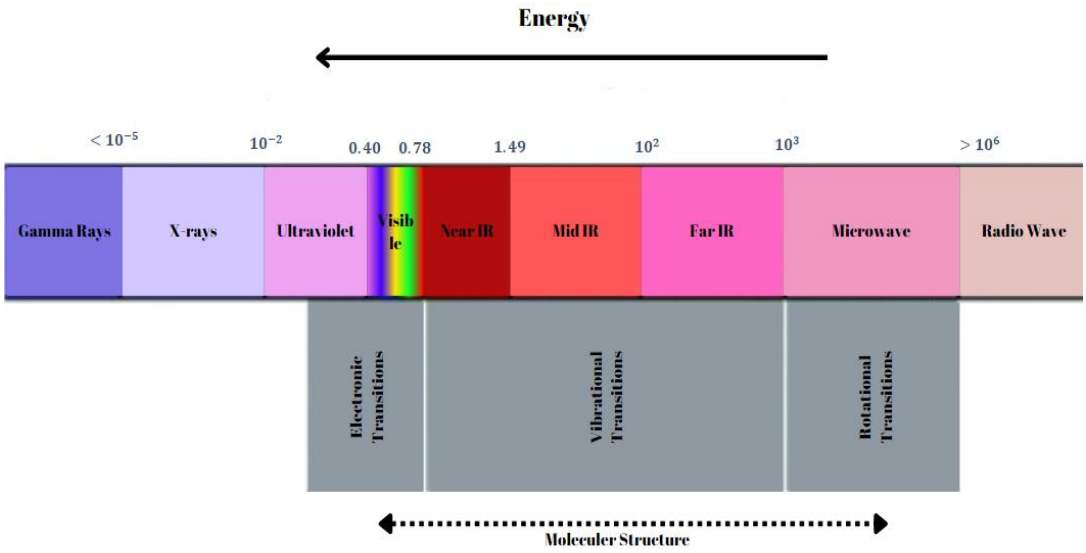


**Figure 1.1:** Electromagnetic spectrum graph. Adapted from [2].

For non-ionizing light skin penetration depth is wavelength-dependent [3], [4]. Typically, light with wavelengths in the visible to NIR region can penetrate in the range of a few millimeters with a maximum of around 5mm for wavelengths around

800nm [5]. Light penetration depth is important when applying an optical non-invasive scheme for monitoring which necessitates penetration down to the blood vessel network underneath the dermis layer [6]. Thus, most optical non-invasive measurement methods concentrate on the visible to NIR region of the spectrum. Studies outside his region must improve light delivery and detection methods to overcome the loss of signal.

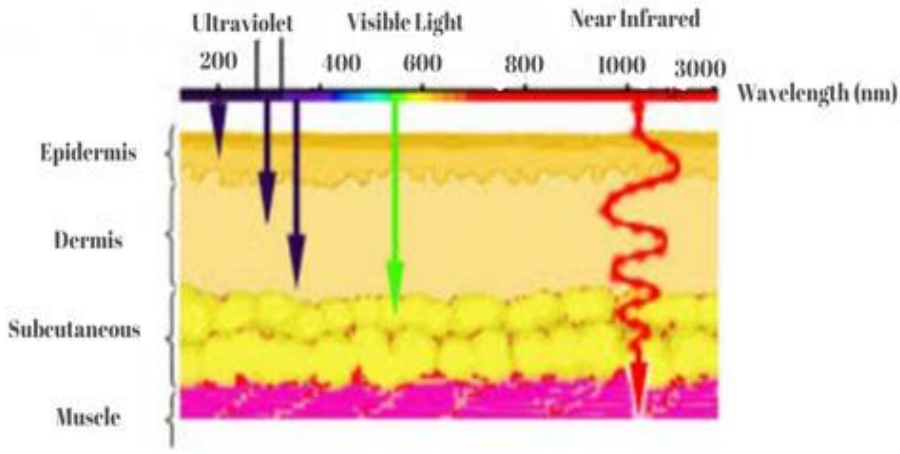


**Figure 1.2:** The characteristic penetration depth in skin for light from the UV to NIR (1/e). Adapted from [7].

Developing such measurement tools requires a comprehensive model that can simulate the interacting light field with different layers in the skin. Approaches based on Monte Carlo statistical methods have proven effective in modeling the light reflectance of skin with improvement in the modeling typically coming from increasing the number of layers from 3 to up to 9 depending on the penetrating wavelength [8]. Using in-vitro and in-vivo measurements as well as measurements with phantoms researchers have been able to characterize well the absorptive and scattering properties of human skin in the region up to the extended NIR region [8]–[11].

The possibility of applying non-invasive techniques in the extended NIR region has progressed slowly mainly due to the limited development of sources of light and methods based on optical delivery. LEDs based on GaSb and InSb materials have

extremely low efficiency in this wavelength range [12]. Similarly, tunable diode lasers which can achieve spectral selectivity while offering a low divergent beam suitable for fiber delivery systems are an area that is now seeing some success but is far from realization due to the limited widespread availability of the technology [12]. Lamps offer good spectral coverage in this range but the fiber coupling efficiency of such sources results in weak return signals. Free-space optical solutions are typically applied directly over the measurement area and thus are not attractive due to the inflexible measurement nature. There is room for improvement and recent advancements in MEMS-based optical technologies have allowed researchers to develop tools that can be used for spectral studies in the extended NIR region. MEMS-based Fabry-Perot (FP) wavelength filters are based on the principle of resonant transmission as a function of the gap (cavity) length between two mirrors whose reflectance determines the spectral selectivity of the light at its output [13]. These tunable wavelength filters offer a low insertion loss while offering good spectral selectivity making them useful for applications where collected light power is an issue.

## 1.1 Human Skin Properties

The skin can be defined as a heterogeneous environment consisting of many layers and each layer having optical properties [14]. The structure of the skin depends on factors such as gender, age, and race. Ideally, it is necessary to determine the optical properties of each layer [14]. The skin is structurally composed of three parts. These are the epidermis, dermis, and subcutaneous. Because the layers are composed of different structures, the light is exposed to different optical events in these three layers [14]. All three regions significantly affect the propagation properties of light [15].

### 1.1.1 Epidermis

The epidermis is the outermost layer of the skin and consists of structures that do not contain blood vessels. While the epidermis shows a more forward scattering feature, there are no blood vessels in this part. The approximate thickness of the epidermis is 100μm [16], Its thickness varies between 50–100μm. The epidermis can be divided

into five sublayers: stratum corneum, stratum lucidum, stratum granulosum, stratum spinosum and stratum basale [17].

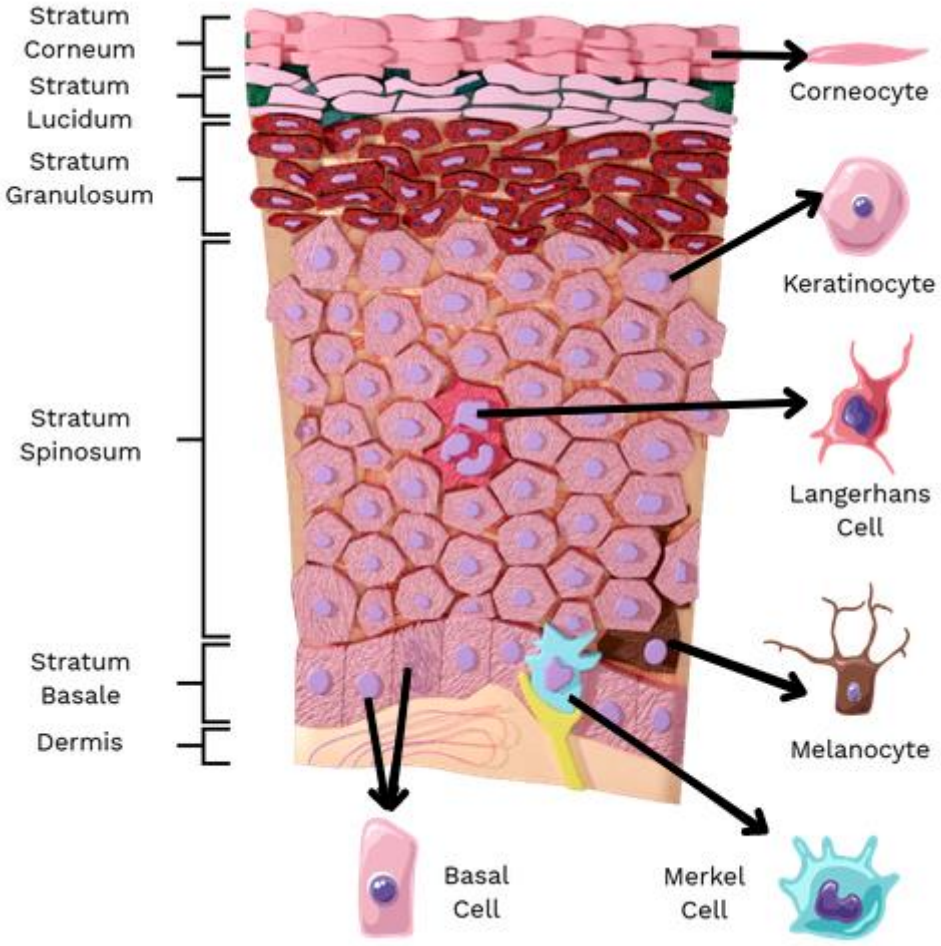


**Figure 1.3:** Structure of Epidermis. Adapted from [18].

**The stratum corneum** is the uppermost layer of the skin in contact with the external environment. The epidermis consists of keratinized scales and keratinocytes. Keratinocytes play an important role in our immune defense system. These structures provide mechanical protection and preserve the integrity of sensitive structures located in the underlying layers [17].

**The stratum granulosum** consists of lamellar granules and keratohyaline granule cells. Basophilic keratohyalin granules in the stratum granulosum give the keratinocytes there an irregular shape [19]. Keratinocytes in the granular layer secrete Odland bodies, lamellar granules and keratinosomes. Secreted substances form a water-permeable barrier and facilitate cell adhesion in the stratum corneum [19].

Between the stratum granulosum and stratum corneum layers is **the stratum lucidum** [20]. It is a smooth and translucent layer [20]. The stratum lucidum is found in thick skin such as the palms, thick skin of the fingers, and soles of the feet [20]. It also consists of dead and squamous keratinocytes [20]. By converting keratohyalin to eleide, a protein-rich in lipids, it gives a transparent appearance and provides a barrier against water [20].

**The stratum spinosum is** known as the spiny cell layer. With its irregular and polyhedral cells with cytoplasmic processes, it can contact neighboring cells. Keratinocytes are found in the stratum spinosum and these keratinocytes initiate keratin synthesis and help secrete glycolipids that prevent water loss. In the stratum spinosum layer, there are dendritic cells between the keratinocytes. Dendritic cells destroy bacteria, damaged cells and foreign particles [17].

**The stratum basale** is located in the epidermis and is the thickest layer [20]. This layer connects the basal lamina, where the dermis layers are located to the epidermis [17]. The cells in this layer are connected to the dermis by intertwined collagen fibers called the basal membrane [17]. The dermal papilla on the surface of the dermis increases the connection strength between the epidermis and the dermis [20]. The stratum basele consists of melanocytes, merkel and basal cells [17]. Basal cells are cuboidal-shaped stem cells that produce keranocyte [17]. Keratinocytes, on the other hand, constantly produce new cells [20]. Also, a large amount of melanin is found in the stratum basel, which is the outermost layer of the skin [17]. Melanin is the main absorbent in the epidermal layers and has strong absorption. It can also scatter most of the absorbed ultraviolet radiation. When exposed to ultraviolet radiation, the skin initiates melanin synthesis as a defense mechanism against this damage [21]. Since the epidermis forms the outermost layer of the skin, mela is most concentrated in the stratum basele. Because of this feature, it plays an important role in the visual characteristics of the skin, such as skin spots and skin tone. Melanin is an important absorber in the skin, so it effectively scatters most of the absorbed ultraviolet radiation [17]. While the stratum corneum has a crucial role in the preservation of skin moisture, the moisture level within the epidermis is also a significant determinant of its thickness [14].

### 1.1.2 Dermis

The dermis lies below the epidermis and consists of dense irregular connective tissue. Epidermis represents the thickest layer among the three skin layers. [8], [15]. The approximate thickness of the dermis is 1-4mm [14]. The dermis layer mostly contains fibers, vasculature, and collagen. Collagen fibers found in the dermis are age-related. Lack of collagen fibers causes skin aging and loss of skin elasticity. It can also make the skin more vulnerable to damage [22]. The fact that the dermal layer has a high water content and a wide capillary network facilitates the transport of alcohol [23]. Measurement of alcohol from subcutaneous tissue to blood is a method used to monitor continuous alcohol consumption [24]. In this method, a device or sensor is implanted under the skin and continuously measures alcohol levels.

The dermis consists of two sublayers, the reticular dermis, and the papillary dermis [20].

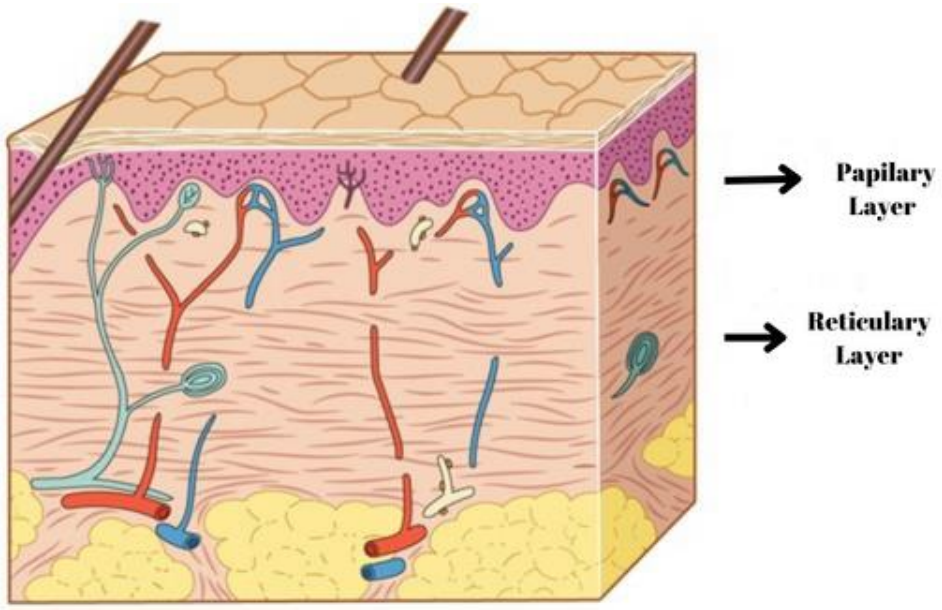


**Figure 1.4:** Structure of Dermis. Adapted from [25].

**The papillary layer** is composed of collogen fibrils and elastic fibers [26]. The surface layer of the dermis touches the epidermis up to the stratum basale, where it gives rise to dermal papillae that resemble finger-like projections [20]. The layer containing small blood vessels and a fine network of collagen fibers is the papillary

dermis. The papillary layer also consists of phagocytes [27]. Phagocytes function as immune cells and defend against bacterial pathogens and infections that threaten the skin [27]. There are touch receptors in the papillary layer. These receptors include lymphatic capillaries, nerve fibers, and Meissner corpuscles [17]. Also, the reason for the formation of fingerprints is caused by the dermal papilla in the papillary dermis [17].

**The reticular layer** is the lowest layer of the dermis and the thickest layer of dense irregular connective tissue. The reticular dermis consists of a thicker fiber network and large blood vessels. In addition, this layer contains glands, hair follicles, lymphatics, nerves, and fat cells [28]. A mesh-like structure of elastin fibers and collagen fibers surrounds the reticular dermis. The presence of elastin fibers, allows the skin to gain flexibility and move [20]. The main absorbing sources such as blood vessels, hemoglobin, carotene, and bilirubin are in this part. The dermis is rich in blood vessels [8], [15]. The blood and water in the dermis are also light-absorbing sources. The main absorbent of the dermal layer is blood. The blood volume fraction within the dermis ranges between 0.2 % and 7 % [29].
The reticular dermis is the third layer of the skin and forms a border with the hypodermis. The hypodermis contains a large amount of lipid cells. This layer is 4 - 9 mm thick [30].

### 1.1.3 Subcutaneous

The hypodermis refers to the deepest layer of the skin and is known as the subcutaneous layer or subcutis. It consists of fat cells. The task of the subcutis layer is to protect and support the nerve and vascular network in the tissue from external factors (heat and impacts) [31]. The approximate thickness of the subcutaneous fat layer is 1-6 mm [14].

## 1.2 Optical Methods for Detection of Glucose, Alcohol, and Blood Parameters Detection: A Background Review

The use of near infrared light is preferred to measure light absorption in thicker tissues [32]. The near-infrared light region is commonly preferred for absorption assessment due to its suitability for thicker tissue sample measurements [33]–[35]. Transmitted or reflected light in human tissue is affected by parameters such as hemoglobin concentration, blood flow, oxygenated hemoglobin saturation, hematocrit, arteriovenous oxygen difference [36]. Nowadays, easy, fast, cost-effective and safe monitoring can be done with optical techniques. For this reason, NIR and Ex-NIR region research areas are of critical importance today. Many researchers use the ability of near-infrared light to penetrate the skin and reach subcutaneous tissue to provide glucose information [14]. The in vivo measurement method commonly used in glucose, alcohol and pulse measurements is an optical method. Diagnostic methods used in medicine depend on optical phenomena such as reflection, transmission, absorption and scattering of light in blood and tissues.

Techniques such as pulse oximetry, blood oximetry, tissue oximetry and in vivo-in vitro measurements are among the oximetric techniques. The absorption parameter is important in oximetric techniques. Oxygenation parameters are obtained by optical attenuation measurements. The most important point of these measurements is the separation of absorbed and scattered components from the general attenuation phenomenon. To accurately evaluate oxygen saturation, it is important to separate the absorbed and scattered components from the attenuation phenomenon [37]. In order to completely comprehend the mechanisms of light scattering and absorption in tissue and blood, one of the oximetry techniques, known as pulse oximetry, is crucial to the creation of diagnostic instruments. The oxygenation of the blood is measured using a pulse oximeter using an optical sensor to determine the oxygen saturation (SpO2) and pulse rate. This sensor typically comprises of photodetectors and a light source. The tissues near the skin are penetrated by LED light. Depending on the existence of oxygenated hemoglobin (red blood cells coupled to oxygen) and deoxygenated hemoglobin (blood cells deprived of oxygen), blood arteries absorb and reflect light in different ways [37]. Oxygenated hemoglobin absorbs red light and reflects infrared

light, while deoxygenated hemoglobin absorbs both red and infrared light. Optical methods such as Raman spectroscopy and Spectral reflectance have been investigated and widely used in glucose measurements [38]. Raman spectroscopy is a method for learning about the molecular structure of molecules by using the interaction of light with those molecules, such as glucose. Raman spectroscopy is a technique that may be used to measure the levels of subcutaneous glucose. This technique uses a laser to illuminate the skin, and the spectra of reflected or scattered light is analyzed to determine the glucose levels [38]. Another technique that makes use of the optical characteristics of glucose molecules under the skin is spectral reflectance. In order to measure glucose levels, this technique uses a light source that generates light at various wavelengths and analyzes the spectral characteristics of the light reflected from beneath the skin [39]. These optical methods have potential for glucose measurement. Studies need to be developed to increase the reliability and applicability of these optical methods [39]. Additionally, experimental and simulation studies are required to evaluate performance and accuracy.

Measurement of alcohol from subcutaneous tissue to blood is a method used to monitor continuous alcohol consumption [24]. This approach involves inserting a sensor or gadget beneath the skin to continually measure the alcohol level. It is possible to assess blood alcohol levels from subcutaneous tissue using optical techniques. Alcohol may be quickly and painlessly detected from subcutaneous tissue using optical techniques. These techniques use the interplay of light reflected or transmitted by alcohol molecules to detect alcohol. Here are some optical methods:

Infrared Spectroscopy: Infrared light at certain wavelengths interacts with alcohol molecules [40]. Analysis of the skin's infrared light absorption patterns using infrared spectroscopy allows for the detection of alcohol [40]. The presence and concentration of alcohol can be detected by this method. Spectroscopic methods can be used in the near infrared (NIR) and extended near infrared (Ex-NIR) region. Typically, the range from 700 to 2500 nanometers (nm) is commonly defined as the NIR region [40]. The typical absorption zones of organic substances, such as alcohol, are covered by the NIR spectrum.

Surface Plasmon Resonance: Alcohol molecules on a certain surface interact with surface plasmons to cause changes, which is how surface plasmon resonance works [41]. Surface plasmon resonance is affected by the presence of alcohol, and this change can be used for alcohol detection.

Raman Spectroscopy: Alcohol is found utilizing the spectrum fingerprints of alcohol-related Raman scattering in Raman spectroscopy. When it comes into contact with the skin with laser light, it interacts with alcohol molecules and scatters. The scattered light causes a unique spectral pattern that reflects the presence and concentration of alcohol [42].

Fluorescence Spectroscopy: Excitation of alcohol molecules at particular wavelengths and detection of the fluorescent light that results are the foundation of fluorescence spectroscopy [43]. In the presence of alcohol, the amount of fluorescent light changes, so alcohol detection studies can be performed with this change. These optical methods can be used for non-invasive measurements and can allow real-time results to be obtained. However, factors such as skin type, pigmentation, and environmental conditions may affect the accuracy and reliability of these methods. Extended near infrared (NIR) wavelength range is 1.4 to 2.5 micrometers (μm) [44]. This range help to penetrate deeper tissues. Optical methods in the extended NIR range may be more suitable for alcohol detection in deep tissues. However, each method has advantages, disadvantages and accuracy levels, so there are factors that need to be considered depending on the application areas.

## 1.3 Scope of Thesis

To determine how human skin responds in the extended infrared region, the optical properties of absorption and scattering need to be determined with a suitable experimental measurement set-up and then modeled numerically to obtain the pertinent parameters. In this study by implementing a fiber bundle-based optical measurement system that uses a quartz-halogen lamp light source and a MEMS-based FP tunable wavelength filter coupled with an ex-NIR photodiode the reflectance of

human skin in the 2000-2450nm region was measured and results were simulated using a 3-layer Monte Carlo model to obtain estimates for the optical parameters.

The approach outlined here is based on understanding the simulation's quality compared to the experimental data and published data which it is based on for the well-studied NIR region reflectance of human skin. Due to the windowed measurement range of the Fabry-Perot filter the focus is placed in the 1550-1950nm region, where there are many published results [9], [11] which give parameters for skin reflectance from various layers of the skin.

Human skin is composed of three layers: the subcutaneous layer, the dermis, and the epidermis [12]. Each of these layers consists of components with their optical properties. The simulations are based on a three-layer skin texture model that utilizes Monte Carlo (MC) methods to estimate the reflected light from different layers of the skin. The main required parameter values that must be specified to run the MC simulation are the refractive index, the absorption coefficient, the scattering parameter, anisotropy, and thickness parameters in each of the three layers. After analyzing the literature values for refractive index, absorption, scattering coefficient, anisotropy, and thickness of each layer at 50nm intervals steps were determined for different layers of the skin in the 1550-1950nm wavelength range. These parameters were then fed into a Monte Carlo based algorithm which estimates the number of scattered and reflected photons and thus the reflectance at each wavelength step. After verifying these parameters in the NIR region a similar skin model was used to assess the parameters that govern the propagation of light in the ex-NIR region. The region in question is again based on the measurement window of the Fabry-Perot filter, namely 2000-2450nm. The thicknesses for the stratum corneum, epidermis, and dermis were kept constant for both simulation regions. Furthermore, the depth in each layer is governed by the absorption due to water for that spectral region [13]. This is especially true in the extended infrared region absorption spectrum measured on the skin, where water absorption predominates over other components [13]. The relevant absorption and scattering coefficients are characterized according to average water content in the tissue of at least 70% in each layer [15], [45].

# CHAPTER 2

# BACKGROUND

## 2.1 Optical Measurement of Human Skin

The electromagnetic radiation that makes up light is a type of energy. Visible light, microwaves, ultraviolet rays, infrared rays, etc. can be expressed as light is separated by wavelength and measured in nanometers (nm) [46].

After the discovery that sunlight is separated into colors by a prism, the behavior of light was accepted as waves, and the classical electromagnetic theory was published. After the discovery of wave properties, the particle behavior of light was discovered. Thus, wave-particle duality was proposed. A stream of particles called photons was proposed by Einstein [47]. The concept that photons are particles of light has taken its place in the world of physics. With this photon concept, the foundations of geometric optics were laid by [47]. Geometric optics helps us better understand the transmission, reflection, absorption, and scattering properties of light.

Light can behave in three different ways when it hits a surface: it can be reflected, transmitted, or absorbed. Reflection is the backscattering of light in the direction it came from. Transmission refers to the state in which light passes through a medium. Absorption refers to the situation in which light is absorbed by an object and some of it is retained [47].

It is important to evaluate optical properties such as distribution, scattering, transmission and reflection of light within human skin. Light arriving at the human body interacts with various components in the tissue, causing processes such as absorption, reflection, scattering or transmission [45]. The skin has a complex structure and optical properties that vary according to individuals. The factors affecting the interaction of light and blood are wavelength of light, biological tissue,

tissue optical properties, refractive index, absorption coefficient, and scattering coefficient. Therefore, the optical properties are not homogeneous. The interaction between light is more complicated due to various substances in the blood, transmission, absorption, and scattering of light are the main phenomena [45].

Reflection measurements are obtained by transforming the parameters characterizing the light emission in the tissue. The transformation process is based on a certain theory of light transmission in tissue [15].

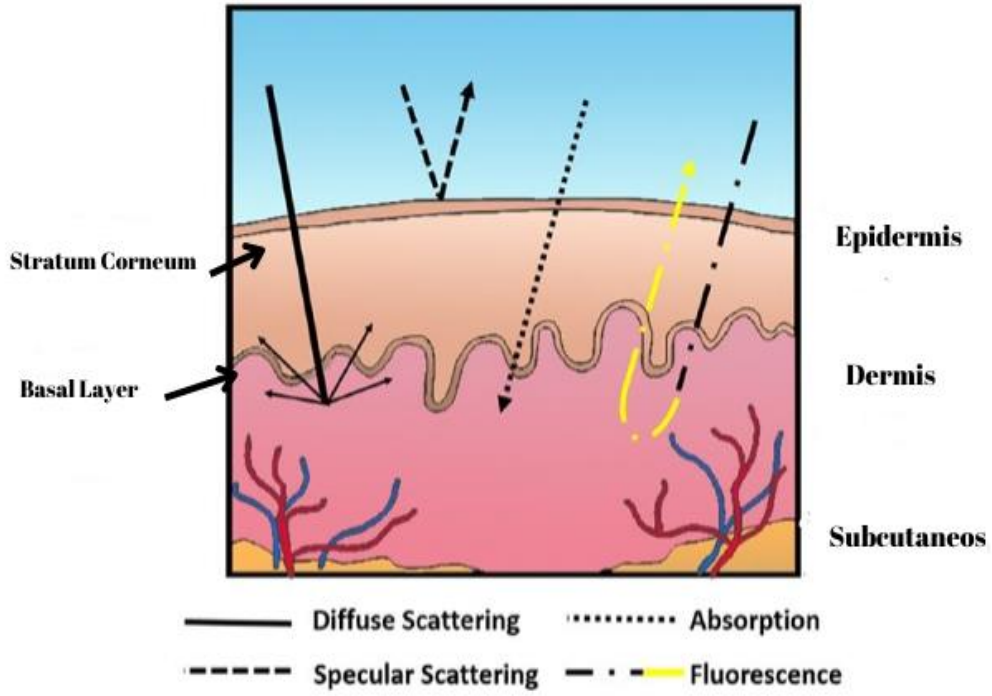


**Figure 2.1:**Schematic representation of reflection, absorption, and scattering phenomenon. Adapted from [48]**.**

When light hits a smooth surface, reflection in one direction is called specular reflection. Since the angle of incidence is equal to the angle of reflection, it preserves the reflected light intensity. In specular reflection, incoming light rays are characterized by a reflective surface as they reflect from the surface at predictable angles. Specular reflection is essential for the formation of clear images as light reflects off a surface without significant distortion [49].

To determine how light interacts with the skin and to understand human skin optical approaches, first it needs to understand the two phenomena of the optical properties of human skin and absorption and scattering light emission. In recent years, it has reported values for effective refractive index, anisotropy factor, absorption, and scattering coefficients for tissues at various light wavelengths. It was observed that the skin layers were effective in determining these values.

When light encounters an irregular surface, scattering occurs in many directions, this phenomenon is defined as diffuse reflection. In diffuse reflection, the surface is seen as non-reflective because the incoming light is reflected from various angles. The intensity of the reflected light is directly proportional to the angle's cosine between the surface normal and the incident light's direction. It means that the intensity of the reflected light decreases as the angle of the incident light increases [49].

The light-gathering capability of the device is crucial for accurate optical measurement, making optical measurement an essential tool in biological studies. The term "light-collecting power" describes a lens or objective's capacity to capture light. The term "numerical aperture" (N.A.) is a parameter used to describe how well lenses or objectives in optical systems can gather light. Greater light-gathering ability is indicated by a higher N.A. score. The amount of light present in the samples being measured can be restricted in optical measurements. An optical system may gather lighter and produce higher resolution with a higher numerical aperture.

In diffuse reflection, it is necessary to collect the light in the space with a lens or a spherical mirror. Summing power is done with NA. If the NA is large, the light-gathering power increases. The closer you get to the objective, the lower your light-gathering power, and as it decreases, it is necessary to increase the NA of the lenses.

$$F_{Number} = \frac{f}{d} = \frac{1}{2NA} \qquad 2.1$$

*f=focal length*

*d= diameter*

Large inner diameters and high numerical aperture (NA) values are essential in fiber systems. The fibers' leaving and receiving angles for light are represented by the numerical aperture. High NA values enable fibers to transmit light more effectively and to capture more light from their surroundings, leading to improved efficiency. A high NA value enhances optical signal transmission, resulting in faster and more dependable data transmission. However, it is significant to remember that lowering the NA value can result from boosting the light-capturing capability. Consequently, the inner diameter of the fiber is also significant in a fiber system. Large-diameter fibers assist in transferring lighter and transmit optical messages more effectively.

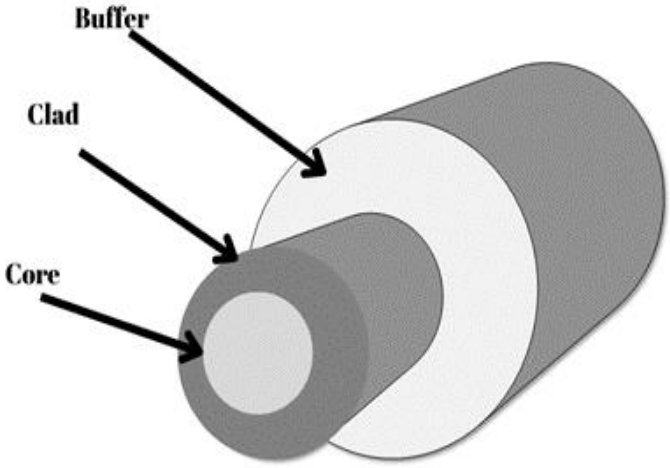


**Figure 2.2:**Structure of Optical Fiber

$$NA = \sqrt{{n_{core}}^2 + {n_{clad}}^2} \qquad 2.2$$

*n: refractive index*

The core refractive index $n_1$ is higher than the cladding refractive index $n_0$. Therefore, total intermal reflection restricts the light beam linked to the wavequide's end face in the fiber. Between the interfaces of the core and cladding, the condition of the total internal reflection is provided by

$$n_1 \sin\left(\pi/2 - \emptyset\right) \geq n_0 \qquad 2.3$$

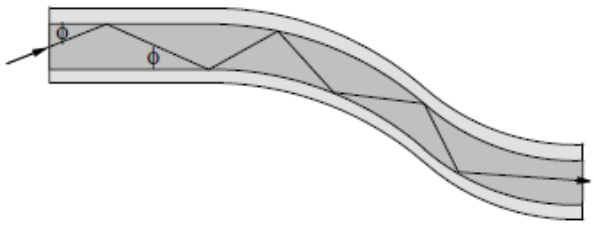


**Figure 2.3:** Schematic representation of the progression of light inside the fiber. Adapted from [50].

Since there is total internal reflection between the core and cladding interference, light is propagated throughout the fiber [50].

The equation $sin\theta = n_1 sin\emptyset \leq \sqrt{n_1^2 - n_0^2}$ describes the relation between the angle and incident beam angle. This equation gives us the essential requirement for total internal reflection (Figure 2.3), which is,

$$\theta \leq sin^{-1}\sqrt{n_1^2 - n_0^2} = \theta_{max} \qquad 2.4$$

Between the core and the cladding, there is a refractive index difference of approximately of $n_1 - n_0 = 0.01$. Using the Eq. (2.3), the $\theta_{max}$ can be obtained as

$$\theta_{max} \cong \sqrt{n_1^2 - n_0^2} \qquad 2.5$$

The waveguide's maximum light acceptance angle is indicated by $\theta_{max}$ and it's known as the numerical aperture (NA) [51].

The maximum angle for propagating light in the core is calculated by $\emptyset_{max} \cong \theta_{max}/n_1 \cong \sqrt{2\Delta}$, where the $\Delta$ is the differences relative refractive index between $n_1$ and $n_0$ obtain from

$$\Delta = \frac{n_1^2 - n_0^2}{2n_1^2} \cong \frac{n_1 - n_0}{n_1} \quad 2.6$$

We obtain the relationship between the relative refractive index difference Δ and the numerical aperture NA by

$$NA = \theta_{max} \cong n_1\sqrt{2\Delta} \quad 2.7$$

Fibers that are designed with a large inner diameter and a high Numerical Aperture (NA) value transmit and collect light more effectively from their surroundings. This implies that the fiber system will transport light more effectively and have a greater capacity for capturing light, resulting in improved performance and results. However, the ability of the fiber to fit within a specific space might also be impacted by a high NA value. Larger diameters are frequently linked to fiber with high NA values. However, the NA value can be decreased by expanding the fiber's inner diameter. Therefore, it is crucial to consider the fiber's ability to fit within the required space while using a high NA value to capture as much light as feasible.

The examples shown in Figures 2.3 and 2.4 illustrate the importance of considering how many fibers can fit in the available space. Firstly, in Figure 2.3, it is assumed that our fiber diameter is 700 microns, and our current area is 1 mm square. In this assumption, the number of fibers that fit in the available space is one. In Figure 2.4, it is shown that when the fiber diameter is reduced to 200 microns, there will be an increase in the number of fibers that fit into the available space.

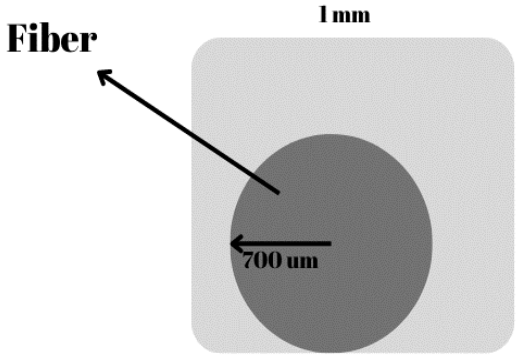


**Figure 2.4**: Example of assumption made with a large fiber diameter.

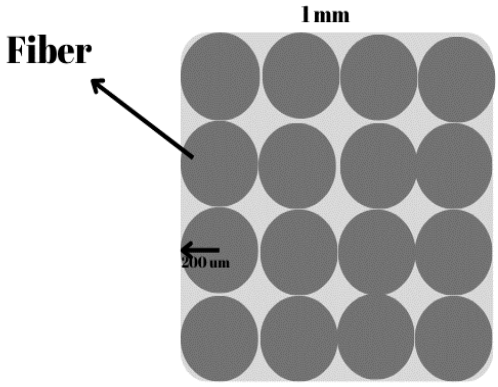


**Figure 2.5:** Example of assumption made with many fibers of small diameter.

As a result, fiber systems with a broad inner diameter and a high NA value enable more effective light transmission and collecting. It is essential to optimize the arrangement of fibers in the field and consider how many fibers can fit in the available space. This has an enormous impact on how fiber systems are designed and optimized.

### 2.1.1 Absorption

The decrease in light energy is defined as absorption. When light interacts with matter, it can transfer its energy to another object or be absorbed. The main event in the propagation of light to the skin is absorption. When light interacts with human skin, it interacts with particles.

An incident light is emitted into the sample. While some of this incoming light is reflected normally, some is absorbed. A decrease is seen in the detected outgoing light.

The Beer-Lambert law (BLL) describes the relationship between the properties of the medium through which the light passes and the attenuation of the light [52]. The absorptive capacity of the substance can be measured by the Beer-Lambert law. BLL is a frequently used method in biomedical optics. The light interaction with the absorption of the medium can be easily measured with this method [52].

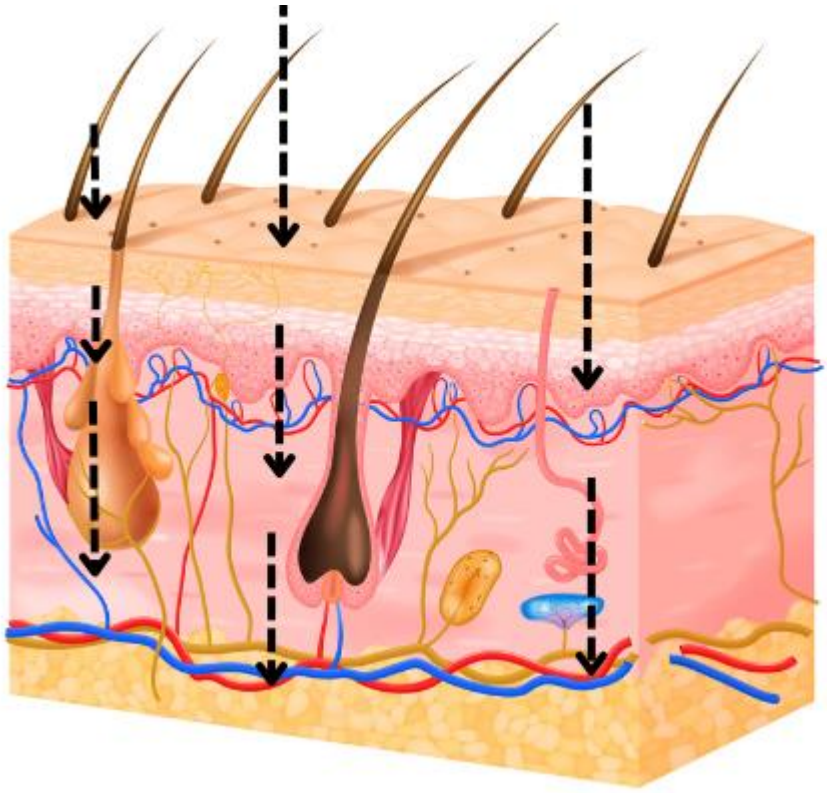

**Figure 2.6:**Schematic diagram of absorption on human skin.

The BLL law can be used to calculate the oxygen saturation of human tissues [53], [54] determine the molar absorbance of bilirubin in the blood plasma samples [55], and determine the concentration or optical path length (OPL) of hemoglobin components [52], [56].

Hemoglobin, melanin, and water are the main sources of optical absorption in biological tissue. The absorption coefficients of several absorbing tissue components are plotted as a function of wavelength [57]. The absorption level of photosensitive

molecules varies according to the wavelength [58]. The absorbance of water in some spectral regions is extremely high [1].

### 2.1.2 Scattering

The change in direction, phase, or polarization of light is defined as scattering. It is also defined as a surface effect, such as reflection or refraction, or interaction with a region whose optical properties are different from its surroundings [59]. The change of direction is defined by the Henyey-Greenstein phase function and the anisotropy factor. The anisotropy factor is described as the cos of the angle between the initial direction of motion of a photon and its direction after scattering [23].

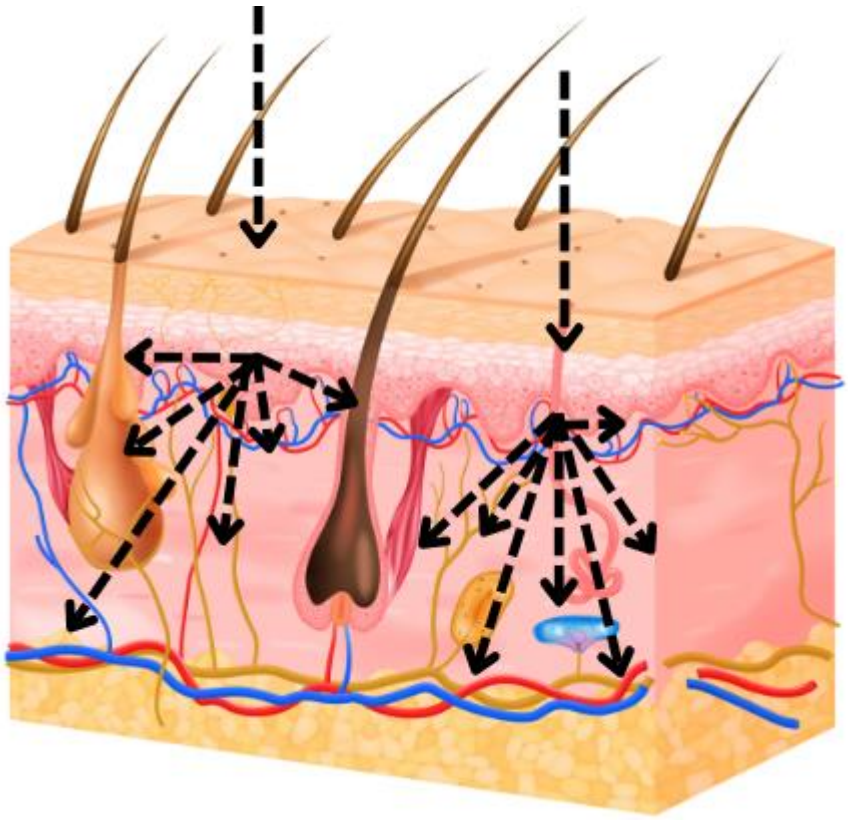

**Figure 2.7**: Schematic diagram of scattering on human skin.

Light interaction in biological structures, ranging from cell membranes to whole cells, causes optical scattering. When photons encounter structures that have a size

comparable to the wavelength of light and a refractive index different from that of the surrounding medium, they experience the strongest scattering. [1]. Variations of refractive index have a significant effect on the scattering of light in tissues. The diffraction variations are determined by the biochemical composition of the tissue and affect the amplitude of the scattered light [14]. Surface and subsurface scattering are the two main components of the scattering profile. Folds in the stratum corneum cause surface scattering, causing 5-7% of the incoming light to be reflected [60]. The rest is transmitted to the internal tissues and two different scatterings occur in the skin layers [61]. These are Mie and Rayleigh scattering. Mie theory or Mie scattering is a mathematical-physical theory of the scattering of electromagnetic radiation by particles of any size. Mie theory is an analytical solution of Maxwell's equations and covers all possibilities of the ratio of particle radius to wavelength [62], [63]. Rayleigh scattering refers to the phenomenon of electromagnetic waves being scattered by particles that are much smaller than the wavelength of the excitation [63].

The level of forward scattering within the stratum corneum and epidermis tissues depends on the wavelength [61] and can be explained by Mie scattering. In addition, fibrous proteins such as collagen and keratin in the skin tissue cause scattering in the human skin [61]. Collagen fibers in the dermis are associated with Mie scattering, other microstructures and smaller collagen fibers are associated with Rayleigh scattering. [61].

The mathematical correlations known as Fresnel's equations describe how light is reflected and transmitted by smooth surfaces. This equation includes Snell's law, which describes how light travels through various media [59]:

$$R = \frac{1}{2}\frac{(a-c)^2}{(a+c)^2}\left\{1+\frac{[c(a+c)-1]^2}{[c(a-c)+1]^2}\right\} \quad 2.8$$

*R=Fresnel reflection*

*$c = cos(\theta_i)$, $\theta_i$, is the angle of incidence*

$$a = n^2 + c^2 \quad 2.9$$

*n is the refractive index of skin.*

$$\theta_t = \arcsin\left(\frac{1}{n}\sin\theta_{\mathrm{i}}\right) \qquad 2.10$$

*$\theta_t$: the angle of refraction at the skin's surface*

The scattering (reflection) and absorption processes within the skin must be considered concurrently. Maxwell's equations, which deal with the interaction between the electric and magnetic fields of light and the structure of matter, can be used to provide a classical explanation for these events. However, this approach becomes challenging to use, especially in the case of complex structures like the human skin, as getting a perfect solution to Maxwell's equations necessitates precise knowledge of every feature in the environment [64].

Radiation transfer theory (RTT), which models absorption as a reduction in brightness, is the most popular approach in the field of skin optics and is based on Maxwell's equations [64]. This theory addresses the subject in its fundamental form and deals with the behavior of light in describing optical phenomena [64].

The scattering coefficient is defined $\mu_s$ (cm′1), volume density $\rho_s$ (cm′3), and $\sigma_s$ is the effective cross-section (cm′2). The scattering coefficient is the cross-sectional area per unit volume [62];

$$\mu_s = \rho_s \cdot \sigma_s \qquad 2.11$$

The anisotropy factor, denoted as g, quantifies the proportion of forward scattering compared to the overall scattering. It is mathematically defined by the following equation. The factor 'g' of anisotropy represents the average cosine value of the scattering angle θ.

$$g = \int p\,(\cos\theta)\cos\theta d\omega \qquad 2.12$$

*$d\omega$: differential solid angle.*

$$g = <\cos\theta \geq \int_0^{\pi} p(\theta)\cos\theta 2\pi\sin\theta\, d\theta \qquad 2.13$$

The scattering phase function, p (θ), characterizes the likelihood of photon scattering occurring within a homogeneous solid angle oriented at an angular displacement relative to the original trajectory of the photon.

Henyey and Greenstein were instrumental in approximating the single scattering in biological tissues to the angular scattering dependence for p(θ)[65]. The Henyey-Greenstein function is defined as [65]:

$$p(\theta) = \frac{1}{4\pi} \frac{1 - g^2}{(1 + g^2 - 2g\cos\theta)^{3/2}} \quad 2.14$$

$$g = < \cos\theta \geq \int_0^{\pi} p(\theta)\cos\theta 2\pi \sin\theta \, d\theta \quad 2.15$$

We can define the reduced scattering coefficient $\mu_s$:

$$\mu_s' = \mu_s(1 - g) \quad 2.16$$

The scattering coefficient is $\mu_s$ and the anisotropy factor is g. The $\mu_s'$ is useful in the diffusion regime that often occurs when treating the propagation of visible and near-infrared light through living tissues [62].

## 2.2 Monte Carlo Analysis Method

The Monte Carlo method is an approach used to solve future modeling problems. Monte Carlo, as the name suggests, is based on "dice rolling" in the sense of tracking a single packet of photons propagating through a turbid substance. A collection of functions or probability distributions that specify the likelihood of the sample's stride measurement of scattering angles and length are used to sample random numbers to estimate the route of each photon packet. MCML (Monte Carlo Multi-Layered) is Monte Carlo modeling of photon transport of a light beam in multilayered tissue [66].

L. Wang invented the Monte Carlo method, which is now commonly used to simulate light propagation through dense, randomly diverse, highly absorbing, and scattering media like skin tissue. According to Wang, a tiny light beam contacts the surface of biological tissue perpendicularly and expands out in the manner described below:

establishing origin trace points based on incident conditions, generating photon path lengths, directions of travel, and nearest impact locations, and identifying transmission at medium borders and scattering or absorption events. Since direct analytical and numerical solutions are heavily constrained by the complexity of the boundary conditions, the Monte Carlo approach is a useful tool for modelling the propagation of light through biological tissues [67]. The Monte Carlo method has been chosen by many researchers as the primary tool for modeling the propagation of optical radiation in biological tissues.

Sampling and simulation, estimating quantities by Monte Carlo simulation, optimization, Bayesian interference, learning and model estimation, and visualizing the landscape can be listed as Monte Carlo analysis methods [68]. The Sampling and Simulation process aims to simulate the "typical" microscopic state of the system. With this method, the adequacy of the model is verified by [68]. Estimation Quantities by Monte Carlo simulation calculates by summing (integration) the color and intensity of each pixel in the viewing plane overall light sources from which a beam can be withdrawn from the pixel and various objects to the source [68]. The Optimization and Bayesian Interference Monte Carlo method is suitable for optimizing large-scale complex systems [69]. Learning and Model Estimation produces samples experienced in the Monte Carlo analysis method and then, based on the average return, the value is calculated for a state or state-action [68]. With the Visualizing the landscape analysis method, the behavior of various algorithms can be further visualized and inference or learning difficulties can be quantified [68].

In summary, the Evaluation of optical properties related to light propagation in human skin is significant. Light coming into the skin interacts with various components in the tissue and causes processes such as absorption, reflection, scattering, or transmission. The skin has a complex structure and optical properties that vary depending on the individual. Factors affecting the light interaction with blood include wavelength of light, biological tissue, tissue optical properties, refractive index, absorption, and scattering coefficient. Therefore, the optical properties are not homogeneous. Interaction with light becomes complicated by numerous factors originating from blood and other substances, and transmission, reflection, absorption, and scattering

appear as the main phenomena. The Monte Carlo method is widely used for modeling light propagation. This method provides a practical tool for simulating the propagation of light in biological tissues. Monte Carlo analysis methods include sampling and simulation, quantity estimation, optimization, Bayesian inference, learning and model estimation, and landscape visualization. The Monte Carlo method is preferred as the primary tool for modeling the propagation of optical radiation in biological tissues.

# CHAPTER 3

# MEASUREMENTS

## 3.1 Experimental Set-up

A Thorlabs model SLS201L broadband light source was used to provide illumination in the spectral regions 1550-1950nm and 2000-2450nm. The light source is shown in Figure 3.1. To filter the light in these two spectral regions a silicon plate was used to cut off the portion of the spectrum below 1.1um. An additional bandpass filter with a center wavelength at 2250nm and bandwidth of 500nm was used for the ex-NIR measurements (Thorlabs FB2250-500). The specifications of the measurement scheme are shown in Table 1. A Y-junction Low-OH (Visible to IR) fiber bundle with 19 Fibers in the Common End to measure the diffuse reflected light from the skin (Thorlabs BF19Y2LS02). A detector-coupled Fabry-Perot type tunable etalon (Spectral Engines Nirone Sensor S2.0 & S2.5) was used to measure the spectral content of the diffuse reflectance. The measurement scheme is shown in Figure 3.2.

**Figure 3.1:**Thorlabs SLS201L Light Source

**Table 3.1:** Optical Parameters

| | |
|---|---|
| 19 Fiber Bundle | 0.22NA, 200um core diameter |
| Power on target w/bandpass filter (1550-1950nm) | 6.0mW |
| Power on target w/bandpass filter | 0.4mW |
| Total length | 2m |

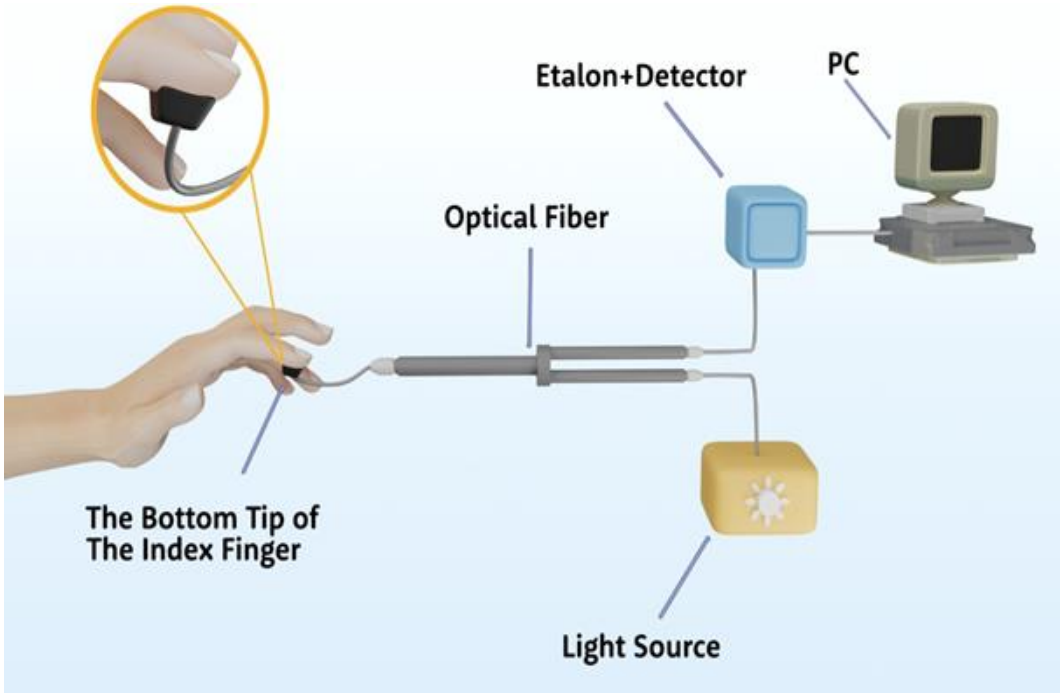


**Figure 3.2:**The Experimental Setup demonstrates recording measurements taken from the bottom tip of the index finger on an etalon+detector using a Thorlabs model SLS201L broadband light source and then analyzing them on a computer.

Measurements were performed by pressing the bundle tip on the distal phalanx of the index finger as shown. Multiple measurements were taken and then averaged. These measurements were recorded for wavelength ranges, 1550-1950nm and 2000-2450nm. The bandpass filter was used to filter the ex-NIR measurements. Measurements were

taken for both wavelength intervals at steps of 10nm with an integration time of 1s. The signal output of the tunable etalon was digitized and recorded with a laptop.

## 3.2 Fabry Perot Principles

The Fabry-Perot interferometer uses the multi-beam interference phenomenon that occurs when light shines through a gap bounded by two parallel reflective surfaces. Two parallel, highly reflective plates called an etalon make up the Fabry interferometer. The light entering the etalon passes through more than one reflection, and the interference of the light leaving the etalon with each reflection causes a modulation in the reflected and crossed rays [70].

The working principle of Fabry Perot is as follows. A Fabry-Perot filter is comprised of an optical cavity formed by two parallel mirrors that are separated from each other. Mirrors are typically distributed Bragg reflectors made up of alternating thick quarter-wave layers of high and low refractive index materials [13]. The maximum optical transmission of the filter occurs at the resonant wavelength, which is twice the optical cavity's length during first-order operation. Phase changes in the mirror reflection are ignored during this process [13]. At wavelengths other than the resonant wavelength, the optical transmission decreases rapidly from its peak resonance value, resulting in the formation of distinct transmission passbands with spectral separation. By employing electrical stimulation to manipulate the spacing of mirrors, it becomes possible to sweep the transmission passband across a range of wavelengths, thereby achieving an electrically tunable optical filter [13].

Fabry-Perot-based MEMS-type tunable wavelength filter is used to measure the scattering and absorption parameters of human skin in the extended NIR region. For this reason, in our study, a Fabry-Perot-based MEMS-type tunable wavelength filter was used.

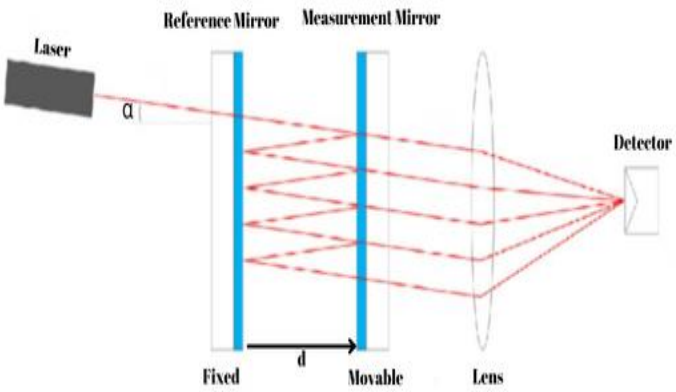


**Figure 3.3:**Fabry–Perot interferometer. Adapted from [71].

An angle between a narrow monochromatic beam emanating from a laser source and the optical axis is seen in Figure 3.3. Within the interferometer, this beam causes the production of several coherent beams. The focal plane of a zooming lens, point d, is where this collection of parallel rays is merged.

$$2d\cos\alpha = m\lambda \qquad 3.1$$

*m is an integer*

*d: distance between two parallel mirrors*

## 3.3 Measurements

Using a Fabry-Perot-based MEMS-type tunable wavelength filter, measurements were taken from 4 separate locations on the arm of the subject. These places were chosen as the top of the index finger (Proximal Interphalangeal), the bottom tip of the index finger (Distal Interphalangeal), the inner hairless part of the forearm, and the top of the hand (Trapezium). While they are all similar, measurements taken from under the index finger were used in our study.

To obtain the reflectance a reference measurement was taken at the common end of the bundle fiber using a highly reflecting silver mirror positioned in a way that the reflected light was maximized and was taken for each measurement. First, 1550-1950

nm measurements were performed. These measurements were first taken as a reference measurement using a mirror without using a filter, and then measurements were made from four different regions on the subjects. For 2000-2450 nm, a Fabry-Perot-based MEMS-type tunable wavelength filter was added to the measurement setup. Firstly, reference measurements were taken with a highly reflective silver mirror, and then measurements were performed on the subjects in 4 different areas. Reference measurements were taken again for each measured region.

The results were processed in the Origin file and the normalization process was performed to prevent data duplication, data loss, and data shortage in our database. Since the coupling of the silver mirror, we used to be not sufficient, we experienced a loss of 85%-90% in our signals. First, our data was normalized and the losses in the optical system were removed.

However, all measurements were performed at room temperature (~20 °C) and using the same methods.

The following Figure 3.4 and 3.5 measurements show the results taken under the index finger.

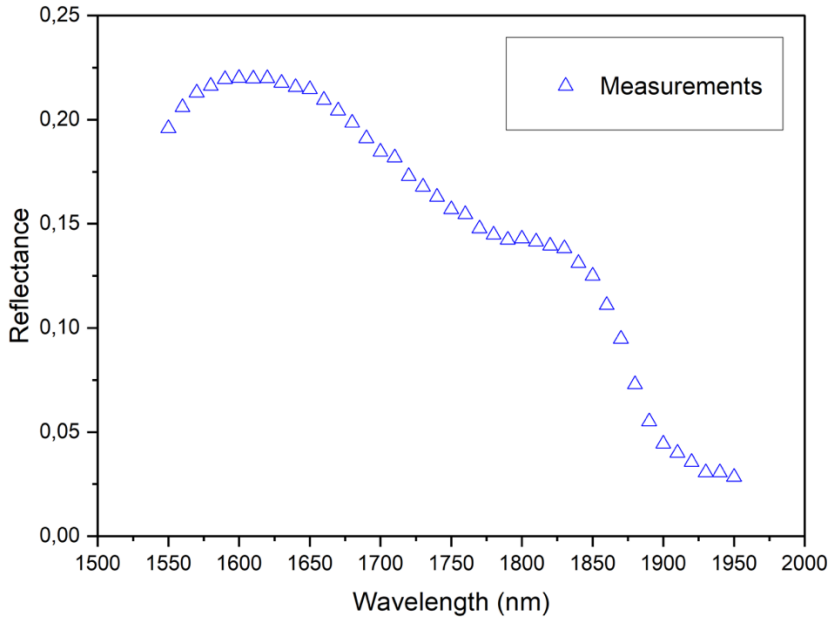


**Figure 3.4:**Measured reflectance data for human skin in the 1550-1950 nm spectral regions.

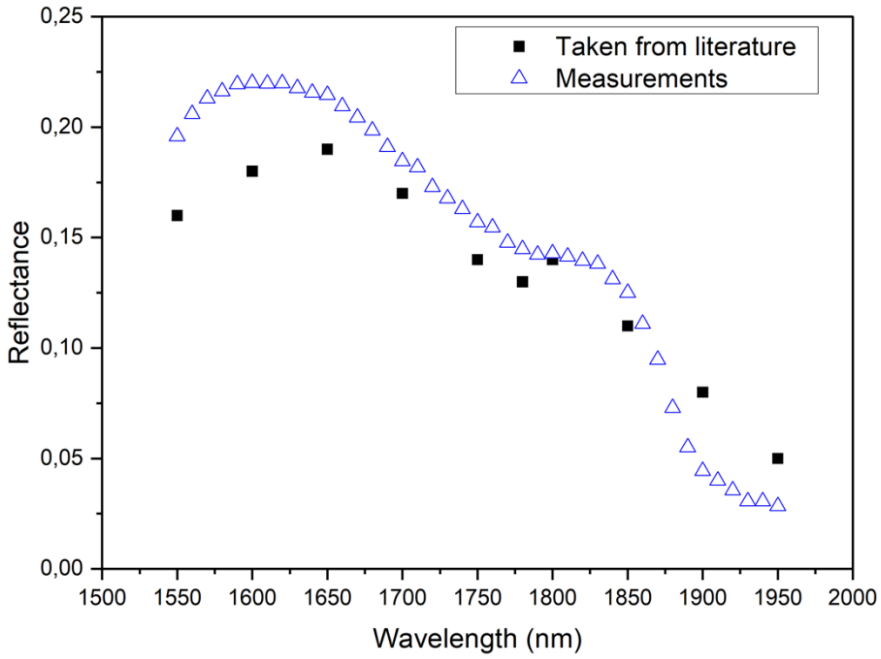


**Figure 3.5**: Comparison of measured reflectance data and published reflectance values in 1550-1950 nm.

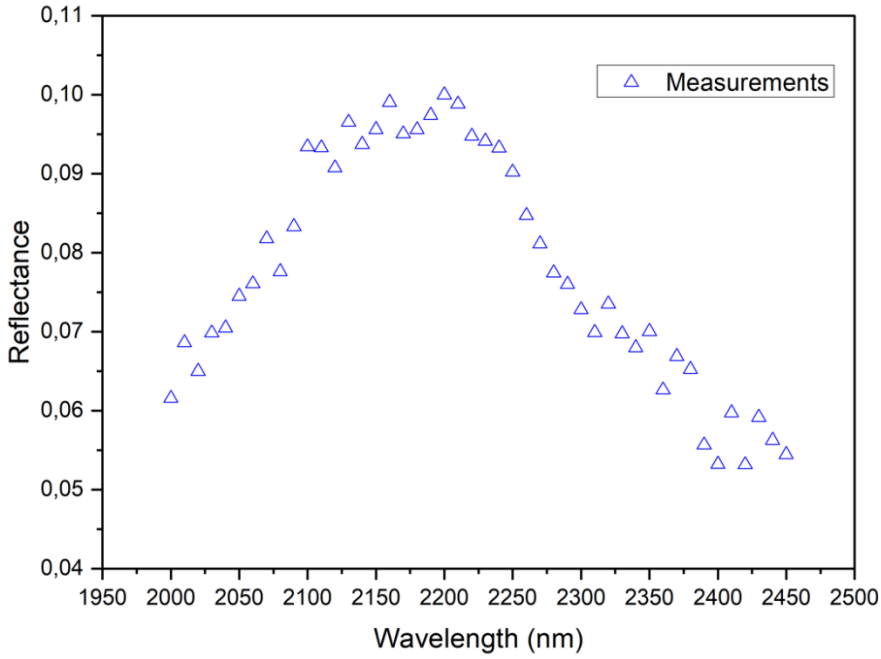


**Figure 3.6:** Measured reflectance data for human skin in the 2000-2450 nm spectral regions.

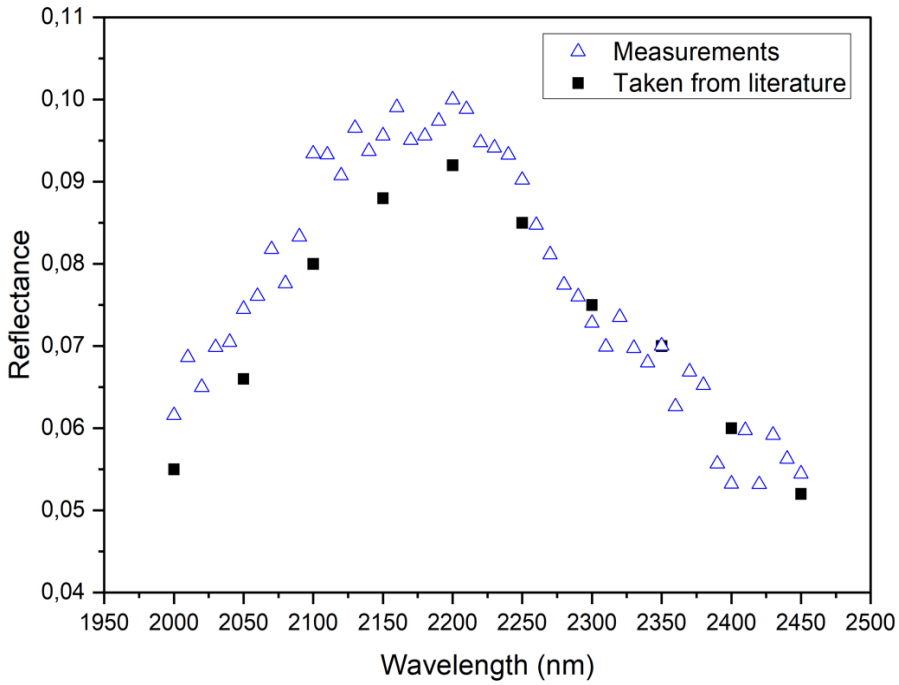


**Figure 3.7:** Comparison of measured reflectance data and published reflectance values in the 2000-2450 nm.

In addition, both female and male subjects with different skin colors were used to understand parameters such as gender and skin color. Measurements were taken from four different regions of these subjects: the top of the index finger, the lower tip of the index finger, the inner part of the forearm, and the upper hand. There is no significant difference was observed in the measurements made between men and women.

Based on Moller, Poulsen, and Wulf's article, it was observed that male skin is thicker than female skin, but in our measurements, this was not so much [72]. There is no significant difference observed in the measurements made. According to these results, parameters such as gender, skin color, and age were ignored in our study.

# CHAPTER 4

# MONTE CARLO SIMULATIONS

## 4.1 Details of Simulations

The Monte Carlo method is a strategy utilized for resolving forthcoming modeling issues. As the name implies, Monte Carlo is based on "dice rolling" in the sense of following individual photon packets as they disperse through a muddy material. By selecting a set of random integers and applying probability distributions or functions that describe the probabilities of sample step lengths and scattering angles, the trajectory of each photon packet may be calculated [66]. Monte Carlo Multi-Layered (MCML) models the photon transport of a light beam in multilayered tissues [66]. The source code of MCML is often used as a basis for many studies in modeling the reflectance of skin [66].

The MCML code requires five input parameters to be specified at a specific wavelength for each layer: refractive index, absorption coefficient, scattering coefficient, anisotropy, and layer thickness [66].

Input parameters are set as function arguments and all simulation results are presented in a simple MATLAB command line structure. The process is performed at 50 nm in the wavelength range in which we perform the simulation. We tracked 100,000 photon packets at every single wavelength. A more comprehensive depiction of the Monte Carlo algorithm can be found in the existing literature [66], [73], [74].

This code snippet provides detailed instructions on how to utilize the described MATLAB function [66].

**Syntax:**

s= MCML (filename, number_of_photons, layers).

**Arguments:**

filename: The name of the input and output files for the MCML.

number_of_photons: The total count of photons to be used in the simulation. Each layer's properties are represented by five values stored as columns in a matrix. The values include the refractive index (n), absorption coefficient (μa) [$cm^{-1}$], scattering coefficient μs [$cm^{-1}$], anisotropy factor (g), and layer thickness (t) [cm]. The order of these values follows the specified sequence.: [n μa μs g t]

**Output:**

s: The MATLAB structure includes all the simulation results and input parameters. One of the significant fields in this structure is "s.refl_r," which represents the reflectance as a function of the radial distance (r) from the source.

To simulate 100,000 photons, we can use the following commands:

The layers matrix is defined by:

*>> layers_matrix= [refractive index absorption coefficient scattering coefficient anisotropy thickness];*

The simulation (10000 photon packets) is started by the command:

*>> s = MCML ('exercise',100000, layers_matrix);*

The resulting reflectance vs. r can be viewed using the:

*>> plot(s.refl_r);*

A three-layer model simulation is used at 1550-1950 nm and 2000-2450 nm to show the reflection of human skin layers (Figure 4.1).

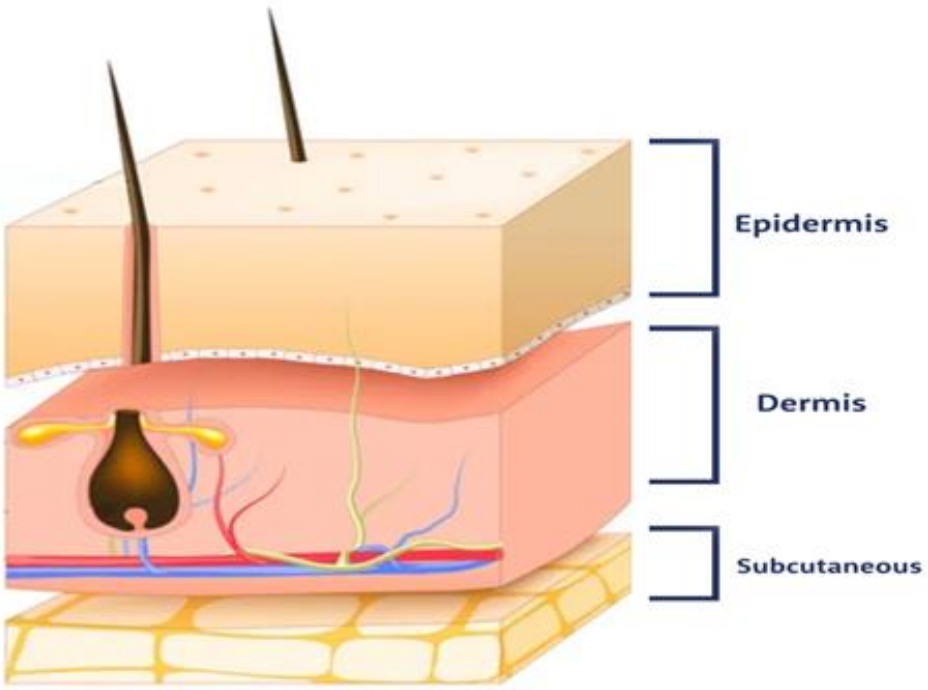


**Figure 4.1**: Schematic structure of three layers of human skin.

## 4.2 1550-1950 nm Region

A careful literature study was carried out to obtain the necessary parameters for the simulation, and this is the determining factor for the wavelength resolution in the simulations. The thicknesses of the epidermis, dermis, and subcutaneous layers are constant for all wavelengths and are accepted as 0.3, 1.2, and 3.0 mm, respectively [9]. Literature values were used for the refractive indices [9]–[11], [16], [75], [76], scattering and absorption coefficients [9], [77], [78]. In the references used, a 3-layer skin model was used, as in our study. Additionally, the experiments in the studies were carried out using phantom. It is important to note that the absorption spectra of skin tissue depend on water and the scattering coefficient decreases with increasing wavelength [79]. In this 3-layer model, the anisotropy is constant and is assumed to be 0.9 for 1550-1950 nm [9], [80].

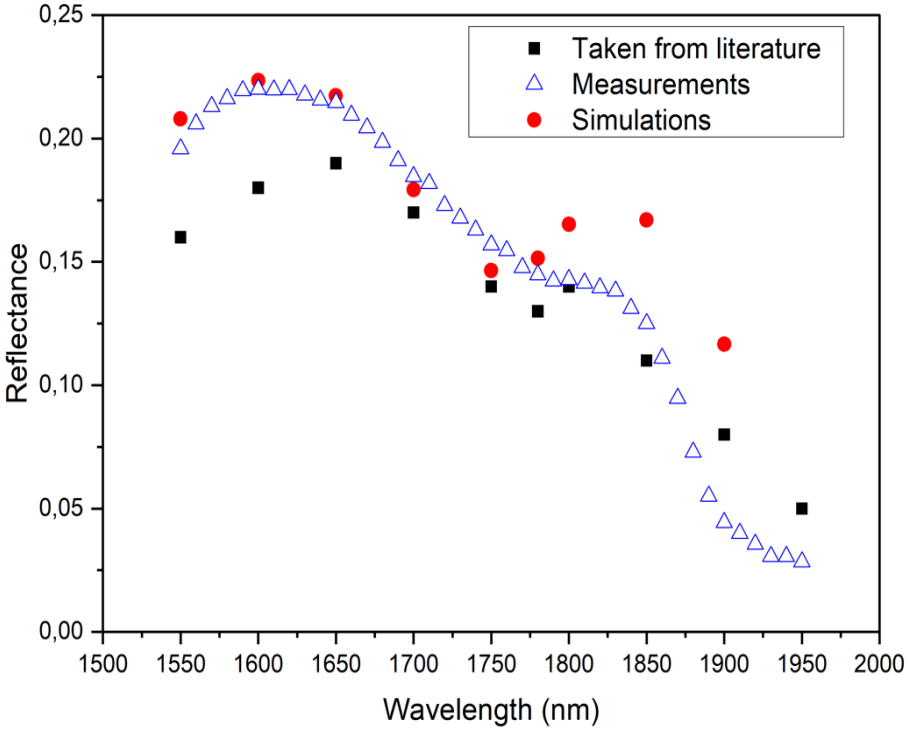


**Figure 4.2:** Measured and simulated reflectance data for human skin in the 1550-1950 nm spectral regions. Black dots showed the reflectance result of Cooksey and Allen [81], [82], red dots our simulation results, and blue dots our experimental measurements.

**Table 4.1:** The skin parameters taken from literature used in the simulation at 1550-1950 nm. The detail of simulations references used are stated in table.

| Wavelength (nm) | Layers | Refractive index | Absorption coefficient (cm^-1) | Scattering coefficient (cm^-1) | Anisotropy | Thickness (cm) [83] |
|---|---|---|---|---|---|---|
| 1550 [11] | Epidermis | 1.34 | 1 | 138 | 0.9 | 0.03 |
| | Dermis | 1.4 | 7.7 | 138 | 0.9 | 0.12 |
| | Subcutaneous | 1.44 | 0.9 | 91.5 | 0.9 | 0.3 |
| 1600 [9] | Epidermis | 1.37 | 1.8 | 136 | 0.9 | 0.03 |
| | Dermis | 1.37 | 5.5 | 136 | 0.9 | 0.12 |

**Table 4.1:** The skin parameters taken from literature used in the simulation at 1550-1950 nm. The detail of simulations references used are stated in table.

| | | | | | | |
|---|---|---|---|---|---|---|
| | Subcutaneous | 1.37 | 1 | 90 | 0.9 | 0.3 |
| 1650 [11] | Epidermis | 1.34 | 1 | 135.9 | 0.9 | 0.03 |
| | Dermis | 1.4 | 4.5 | 135.9 | 0.9 | 0.12 |
| | Subcutaneous | 1.44 | 0.8 | 89.1 | 0.9 | 0.3 |
| 1700 [9] | Epidermis | 1.37 | 1 | 134 | 0.9 | 0.03 |
| | Dermis | 1.37 | 5 | 134 | 0.9 | 0.12 |
| | Subcutaneous | 1.37 | 5.8 | 88 | 0.9 | 0.3 |
| 1750 [9] | Epidermis | 1.37 | 1.5 | 134 | 0.9 | 0.03 |
| | Dermis | 1.37 | 5.3 | 134 | 0.9 | 0.12 |
| | Subcutaneous | 1.37 | 9 | 86 | 0.9 | 0.3 |
| 1780 [11] | Epidermis | 1.34 | 1.5 | 132.9 | 0.9 | 0.03 |
| | Dermis | 1.4 | 6.4 | 132.9 | 0.9 | 0.12 |
| | Subcutaneous | 1.44 | 6.1 | 85.9 | 0.9 | 0.3 |
| 1800 [9] | Epidermis | 1.37 | 1.9 | 132 | 0.9 | 0.03 |
| | Dermis | 1.37 | 6.2 | 132 | 0.9 | 0.12 |
| | Subcutaneous | 1.37 | 5.8 | 86 | 0.9 | 0.3 |
| 1850 [9] | Epidermis | 1.37 | 3 | 132 | 0.9 | 0.03 |
| | Dermis | 1.37 | 8 | 132 | 0.9 | 0.12 |
| | Subcutaneous | 1.37 | 5 | 85 | 0.9 | 0.3 |
| 1900 [9] | Epidermis | 1.37 | 13 | 130 | 0.9 | 0.03 |
| | Dermis | 1.37 | 3 | 130 | 0.9 | 0.12 |
| | Subcutaneous | 1.37 | 15 | 82 | 0.9 | 0.3 |

To compare our simulations with our experimental results, it is necessary to consider the spacing between transmitting and receiving fibers in the bundle used in the experiment. The obtained results of the simulation show the reflectance with distance from the transmitting fiber center. These values were fitted with an exponential decay function and the appropriate reflectance values were exacted for the 0.22mm spacing between fibers in the bundle.

The results of the data measured by [81], [82], simulated and taken from the literature are shown in Figure 4.2. The black dots in Figure 4.2 are described in Cooksey and Allen's article, where the measurement results and reflection properties obtained in the 250-2500 nm wavelength range are described. Experimental studies were conducted in the article and these measurements were taken from the participants' forearm. In our study, the reflection results obtained in this article were determined as the reference point.

The results showed that the measured and simulated reflectance values were similar to other studies published for wavelengths of 1550-1950 nm up to 1800 nm, but after 1800 nm it was observed that our study did not comply with the measured and published values. One of the reasons for this may be that the parameters used in the literature at 1550-1950 nm were studied on phantoms. It can also be assumed that the three-layer skin model is not suitable for this region. Instead of a 3-layer skin model, a 9-layer skin model can be applied.

## 4.3 2000-2450 nm Region

After validating the simulation in the NIR region against experimental results published previously for the 1550-1950nm interval [81], [82], a similar approach was employed to analyze the reflectance of skin in the extended NIR region.

A Fabry-Perot MEMS-based tunable filter was used in experimental research to quantify the reflectance characteristics of human skin in the extended near-infrared (NIR) spectrum. By creating a three-layer skin texture model and selecting the

scattering, refractive index, absorption, and thickness parameters, a skin reflection Monte Carlo simulation was carried out.

The refractive index n is a wavelength-dependent function [8] but the refractive index used in the wavelength range of 2000-2450 nm is assumed to be constant.

Due to water absorption, the penetration of ex-NIR light is limited thus the [83] thicknesses of the epidermis, dermis, and subcutaneous layers were kept the same as the NIR region. These are 0.3, 1.2, and 3.0 mm respectively.

The dermis is a vascularized layer so the absorbance properties in the Ex-NIR spectral range are governed by the absorption of water, while in the visible spectral range the absorbents include blood hemoglobin, and carotene [16]. In the article by Carr, Franke and Bawendi, it was emphasized that the increase in contrast brought by water absorption makes it easier to distinguish and examine the features of deeper layers [84]. Additionally, since water has wavelength-dependent absorption properties, it is vital in determining Ex-NIR optical parameters. This distinction is particularly noticeable for wavelengths where water absorbs more light [84]. In addition, it has an important place in our study since its water absorption at 2000-2450 nm is extremely high.

Additionally, A blood-based assumption was also made for the scattering coefficient since blood's scattering coefficient in the 2000–2500 nm (nanometer) wavelength region is crucial for biological imaging and spectroscopic applications. The blood's hemoglobin has a significant effect on the light it scatters in this wavelength range. Both oxygenated and deoxygenated near-infrared light are absorbed by the pigment hemoglobin. As a result, the amount of hemoglobin in this wavelength range has a considerable impact on the scattering properties of blood [77]. The scattering anisotropy properties of blood were used in our simulation studies, based on the presence of blood vessels in the dermis layer and the greater penetration of light into the dermis layer in the 2000-2450 nm wavelength range. Thus, the scattering coefficient was determined as an average value using the published blood value. It was also assumed that the scattering parameter values at 2000-2450nm were the same for dermis, epidermis and subcutaneous.

In our study, the anisotropy values were determined to be 0.93-0.94 for 2000-2450 nm [80], [85]. For anisotropy values, the blood values in the literature were assumed. These estimates are based on the paper by Roggan, Friebel, Dörschel, Hahn, and Müller [80] who studied the optical behavior of human blood.

Results at a wavelength of 2000-2450 nm were adapted to the 0.22 mm spacing between fibers in the bundle. The simulation results are shown in 4.3.

Figure 4.3 shows the comparison of the results obtained from the simulation, experiment, and literature review.

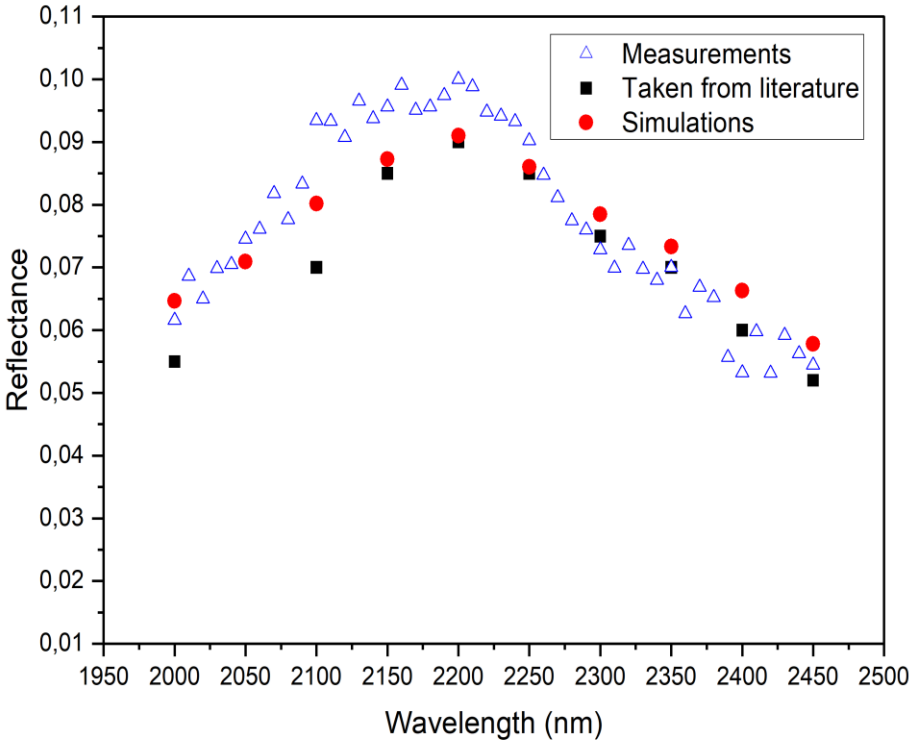


**Figure 4.3:** Measured and simulated reflectance data for human skin in the 2000-2450nm spectral region. Black dots showed the reflectance result of Cooksey and Allen[81], [82], red dots our optimized simulation results, and blue dots our experimental measurements.

As a result, when we compared our simulation and experimental results, it was seen that the absorption coefficient had a significant effect in our study. It was assumed and observed that there was no significant difference between the scattering coefficients

over the entire measured wavelength range. The parameters fit by comparing the experimental and simulation results are presented in Table 4.2 in detail.

**Table 4.2:** Skin Parameters at 2000-2450 nm. The detail of simulations data used are stated in table. While the numbers in red are the data we obtained, black numbers are taken from literature.

| Wavelength (nm) | Layers | Refractive index [80] | Absorption coefficient (cm^-1) | Scattering coefficient (cm^-1) | Anisotropy [80] | Thickness (cm) [83] |
|---|---|---|---|---|---|---|
| 2000 nm | Epidermis | 1.368 | 3 ±0,5 | 50 | 0.94 | 0.03 |
| | Dermis | 1.368 | 3±0,5 | 50 | 0.94 | 0.12 |
| | Subcutaneous | 1.368 | 3±0,5 | 50 | 0.94 | 0.3 |
| 2050 nm | Epidermis | 1.368 | 1.8±0,5 | 50 | 0.94 | 0.03 |
| | Dermis | 1.368 | 1.8±0,5 | 50 | 0.94 | 0.12 |
| | Subcutaneous | 1.368 | 1.8±0,5 | 50 | 0.94 | 0.3 |
| 2100 nm | Epidermis | 1.368 | 1.5 ±0,5 | 50 | 0.93 | 0.03 |
| | Dermis | 1.368 | 1.5 ±0,5 | 50 | 0.93 | 0.12 |
| | Subcutaneous | 1.368 | 1.5±0,5 | 50 | 0.93 | 0.3 |
| 2150 nm | Epidermis | 1.368 | 1 ±0,5 | 50 | 0.93 | 0.03 |
| | Dermis | 1.368 | 1 ±0,5 | 50 | 0.93 | 0.12 |
| | Subcutaneous | 1.368 | 1±0,5 | 50 | 0.93 | 0.3 |
| 2200 nm | Epidermis | 1.368 | 0.8 ±0,5 | 50 | 0.93 | 0.03 |
| | Dermis | 1.368 | 0.8 ±0,5 | 50 | 0.93 | 0.12 |
| | Subcutaneous | 1.368 | 0.8 ±0,5 | 50 | 0.93 | 0.3 |
| 2250 nm | Epidermis | 1.368 | 1±0,5 | 50 | 0.93 | 0.03 |
| | Dermis | 1.368 | 1±0,5 | 50 | 0.93 | 0.12 |
| | Subcutaneous | 1.368 | 1 ±0,5 | 50 | 0.93 | 0.3 |

**Table 4.2:** Skin Parameters at 2000-2450 nm. The detail of simulations data used are stated in table. While the numbers in red are the data we obtained, black numbers are taken from literature.

| | | | | | | |
|---|---|---|---|---|---|---|
| 2300 nm | Epidermis | 1.368 | 1.2 ±0,5 | 50 | 0.94 | 0.03 |
| | Dermis | 1.368 | 1.2 ±0,5 | 50 | 0.94 | 0.12 |
| | Subcutaneous | 1.368 | 1.2 ±0,5 | 50 | 0.94 | 0.3 |
| 2350 nm | Epidermis | 1.368 | 1.6±0,5 | 50 | 0.94 | 0.03 |
| | Dermis | 1.368 | 1.6±0,5 | 50 | 0.94 | 0.12 |
| | Subcutaneous | 1.368 | 1.6±0,5 | 50 | 0.94 | 0.3 |
| 2400 nm | Epidermis | 1.368 | 2.1±0,5 | 50 | 0.94 | 0.03 |
| | Dermis | 1.368 | 2.1±0,5 | 50 | 0.94 | 0.12 |
| | Subcutaneous | 1.368 | 2.1±0,5 | 50 | 0.94 | 0.3 |
| 2450 nm | Epidermis | 1.368 | 2.8±0,5 | 50 | 0.94 | 0.03 |
| | Dermis | 1.368 | 2.8±0,5 | 50 | 0.94 | 0.03 |
| | Subcutaneous | 1.368 | 2.8 ±0,5 | 50 | 0.94 | 0.3 |

The data shown in black in the table are the values taken from the literature, and the data shown in red are the parameters I estimated.

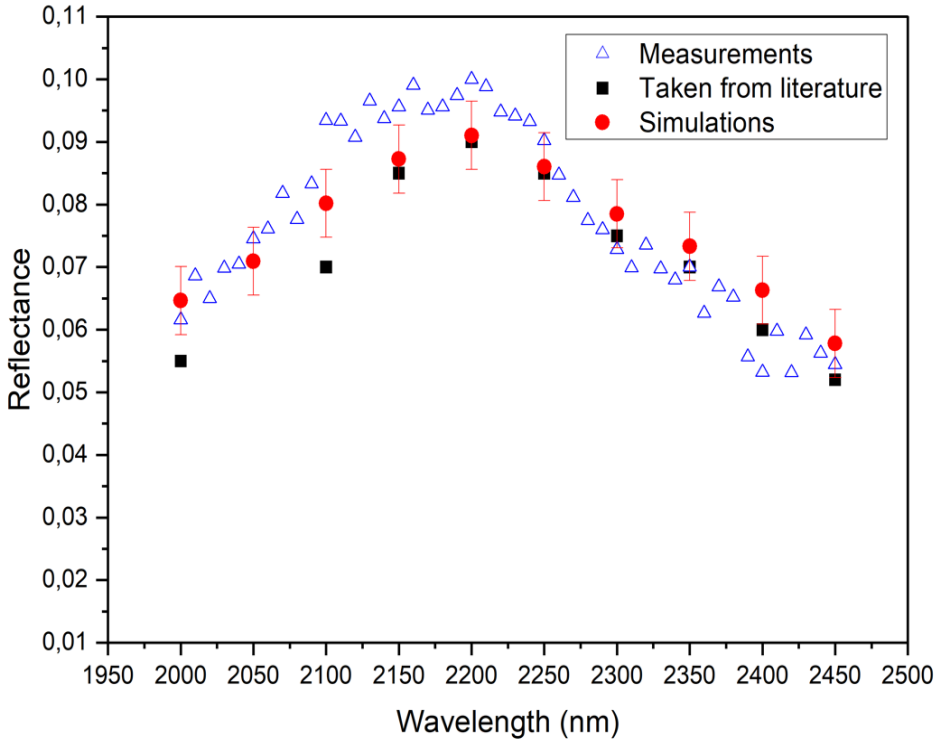


**Figure 4.4:** Comparison figure of data taken from literature results, simulation with error bar added and measurement results.

In Figure 4.5, error bars have been added to the simulation results using the delta method. Thus, it is aimed to reveal the variability of the data. Error bars inserted into data points indicate an error estimate of $\pm 0{,}5$ for each data point.

In addition, the same method was used to reveal the variability of scattering data. Simulations were repeated with an error estimate of $\pm 0{,}5$. Since the standard deviations obtained were very low, no significant difference was observed in the effect of scattering parameters on the simulation.

# CHAPTER 5

# CONCLUSIONS

Our research is based on experimental data for the well-researched NIR region reflectance of human skin and an assessment of the simulation's accuracy in comparison to available data. Epidermis, dermis, and subcutaneous layer are the three layers of human skin. These layers are made up of parts, each of which has unique optical characteristics. The simulations are based on a three-layer skin texture model that uses Monte-Carlo (MC) techniques to determine how much light is reflected from the various levels of skin. The primary parameters that must be supplied in order to conduct the MC simulation are the absorption coefficient, anisotropy scattering parameter, refractive index, and thickness parameters in each of the three layers. The number of scattered and reflected photons, and therefore the reflectivity at each wavelength step, were calculated using a Monte Carlo technique using these parameters.

The optical specifications of the Monte Carlo model are based on limited available literature, especially between 2000-2450nm. A tunable filter based on Fabry-Perot MEMS technology was used to evaluate the scattering properties of human skin in the extended near-infrared (NIR) range. Scattered light was analyzed by Monte Carlo simulation using a multilayer model simulating human skin, and measurement accuracy was evaluated. The research started with careful selection of simulation parameters from the literature, first at wavelengths of 1550-1950 nm. Our experimental work has been completed to verify the design of the simulation results. As a result of the evaluation of the results, it was seen that the Monte Carlo simulation results did not provide a good approximation to the experimental results after 1800 nm. As a result, it can be concluded that our 3-layer skin model is not suitable for 1550-1950 nm wavelength range. It may be necessary to work on more layers for simulations. A 9-layer skin model instead of 3-layer may be more suitable for the NIR region. Another reason may be that the parameters used at 1550-1950 nm in the

literature were studied on phantoms. In our study, experiments were performed in vivo. Thus, it shows that differences in results may occur between in vivo and in vitro experiments.

A comprehensive evaluation of light-tissue interactions at wavelengths of 2000-2450 nm was performed with the same 3-layer skin model method. After comparing and evaluating the simulation, experiment and literature review, we hypothetically derived the absorption and scattering coefficients in Ex-NIR. It has been observed that our three-layer model is more suitable in the Ex-NIR region than in the NIR region.

Our simulation results show that 2150nm and 2200nm are below our experimental results. For this purpose, the simulations were repeated by adding error margins to the absorption and scattering parameters, which are the most important factors. Our results show that, unlike scattering parameters, the absorption parameter is an important factor in human skin reflection. It was observed that the absorption data we obtained was similar to the water absorption profile at 2000-2450 nm. Moreover, this similarity also shows the importance of water in the absorption of human skin in the Ex-NIR region. Based on this, water absorption can be used to match the absorption variability in human skin, thus obtaining more accurate results.

This study presents that MEMS-based devices using the rapidly tunable Fabry-Perot-based spectral measurement technique can be applied for in-vivo research where real-time monitoring is required for accurate analysis. However, it is important to consider the actual skin tissue structure and physiological characteristics in parameter determination.

Future work will focus on improving the link between measured and simulated data to obtain a human tissue model in the 2000-2450 nm wavelength range.

## REFERENCES


[1] L. V. Wang and H.-I. Wu, *Biomedical Optics: Principles and Imaging*. Hoboken, NJ, USA: John Wiley & Sons, Inc., 2009. doi: 10.1002/9780470177013.

[2] C. N. Stedwell and N. C. Polfer, "Spectroscopy and the Electromagnetic Spectrum," in *Laser Photodissociation and Spectroscopy of Mass-separated Biomolecular Ions*, N. C. Polfer and P. Dugourd, Eds., in Lecture Notes in Chemistry. , Cham: Springer International Publishing, 2013, pp. 1–20. doi: 10.1007/978-3-319-01252-0_1.

[3] A. Douplik, G. Saiko, I. Schelkanova, and V. V. Tuchin, "The response of tissue to laser light," in *Lasers for Medical Applications*, Elsevier, 2013, pp. 47–109. doi: 10.1533/9780857097545.1.47.

[4] L. A. Sordillo *et al.*, "Third therapeutic spectral window for deep tissue imaging," presented at the SPIE BiOS, R. R. Alfano and S. G. Demos, Eds., San Francisco, California, United States, Mar. 2014, p. 89400V. doi: 10.1117/12.2040604.

[5] M. D. Francisco *et al.*, "Competitive Real-Time Near Infrared (NIR) Vein Finder Imaging Device to Improve Peripheral Subcutaneous Vein Selection in Venipuncture for Clinical Laboratory Testing," *Micromachines*, vol. 12, no. 4, p. 373, Mar. 2021, doi: 10.3390/mi12040373.

[6] C. Ash, M. Dubec, K. Donne, and T. Bashford, "Effect of wavelength and beam width on penetration in light-tissue interaction using computational methods," *Lasers Med. Sci.*, vol. 32, no. 8, pp. 1909–1918, Nov. 2017, doi: 10.1007/s10103-017-2317-4.

[7] Y. Tanaka, Y. Tsunemi, M. Kawashima, and H. Nishida, "The Impact of Near-infrared in Plastic Surgery," *Plast. Surg. Int. J.*, pp. 1–13, Jun. 2013, doi: 10.5171/2013.973073.

[8] T. Maeda, N. Arakawa, M. Takahashi, and Y. Aizu, "Monte Carlo simulation

of spectral reflectance using a multilayered skin tissue model," *Opt. Rev.*, vol. 17, no. 3, pp. 223–229, May 2010, doi: 10.1007/s10043-010-0040-5.

[9] K. Iino, K. Maruo, H. Arimoto, K. Hyodo, T. Nakatani, and Y. Yamada, "Monte Carlo Simulation of Near Infrared Reflectance Spectroscopy in the Wavelength Range from 1000 nm to 1900 nm," *Opt. Rev.*, vol. 10, no. 6, pp. 600–606, Nov. 2003, doi: 10.1007/s10043-003-0600-z.

[10] H. Arimoto and M. Egawa, "Imaging wavelength and light penetration depth for water content distribution measurement of skin," *Skin Res. Technol.*, vol. 21, no. 1, pp. 94–100, Feb. 2015, doi: 10.1111/srt.12163.

[11] B. Nasouri, T. E. Murphy, and H. Berberoglu, "Near infrared laser penetration and absorption in human skin," presented at the SPIE BiOS, M. R. Hamblin, J. D. Carroll, and P. Arany, Eds., San Francisco, California, United States, Feb. 2014, p. 893207. doi: 10.1117/12.2040337.

[12] T. N. Danilova, "Light-Emitting Diodes Based on GaSb Alloys for the 1.6–4.4 μm Mid-Infrared Spectral Range," *Semiconductors*, vol. 39, no. 11, p. 1235, 2005, doi: 10.1134/1.2128447.

[13] M. Ebermann, N. Neumann, K. Hiller, M. Seifert, M. Meinig, and S. Kurth, "Tunable MEMS Fabry-Pérot filters for infrared microspectrometers: a review," presented at the SPIE OPTO, W. Piyawattanametha and Y.-H. Park, Eds., San Francisco, California, United States, Mar. 2016, p. 97600H. doi: 10.1117/12.2209288.

[14] H. F. Lodish, Ed., *Molecular cell biology*, 6th ed. New York: W.H. Freeman, 2008.

[15] W. F. Cheong, S. A. Prahl, and A. J. Welch, "A review of the optical properties of biological tissues," *IEEE J. Quantum Electron.*, vol. 26, no. 12, pp. 2166–2185, Dec. 1990, doi: 10.1109/3.64354.

[16] A. N. Bashkatov, E. A. Genina, V. I. Kochubey, and V. V. Tuchin, "Optical properties of human skin, subcutaneous and mucous tissues in the wavelength range from 400 to 2000 nm," *J. Phys. Appl. Phys.*, vol. 38, no. 15, pp. 2543–2555, Aug. 2005, doi: 10.1088/0022-3727/38/15/004.

[17] H. Yousef, M. Alhajj, and S. Sharma, “Anatomy, Skin (Integument), Epidermis,” in *StatPearls*, Treasure Island (FL): StatPearls Publishing, 2023. Accessed: Mar. 27, 2023. [Online]. Available: http://www.ncbi.nlm.nih.gov/books/NBK470464/

[18] “Layers of epidermis - Labster Theory.” Accessed: Apr. 10, 2023. [Online]. Available: https://theory.labster.com/epidermis_layers/

[19] J. S. Barbieri, K. Wanat, and J. Seykora, “Skin: Basic Structure and Function,” in *Pathobiology of Human Disease*, Elsevier, 2014, pp. 1134–1144. doi: 10.1016/B978-0-12-386456-7.03501-2.

[20] L. M. Biga *et al.*, “5.1 Layers of the Skin,” Sep. 2019, Accessed: Mar. 27, 2023. [Online]. Available: https://open.oregonstate.education/aandp/chapter/5-1-layers-of-the-skin/

[21] M. Brenner and V. J. Hearing, “The Protective Role of Melanin Against UV Damage in Human Skin†,” *Photochem. Photobiol.*, vol. 84, no. 3, pp. 539–549, May 2008, doi: 10.1111/j.1751-1097.2007.00226.x.

[22] R. Oliver, H. Barker, A. Cooke, and R. Grant, *“Dermal collagen implants,” Biomaterials*, vol. 3. 1982.

[23] L. Finlayson *et al.*, “Depth Penetration of Light into Skin as a Function of Wavelength from 200 to 1000 nm,” *Photochem. Photobiol.*, vol. 98, no. 4, pp. 974–981, Jul. 2022, doi: 10.1111/php.13550.

[24] T. R. Leffingwell *et al.*, “Continuous Objective Monitoring of Alcohol Use: Twenty-First Century Measurement Using Transdermal Sensors,” *Alcohol. Clin. Exp. Res.*, vol. 37, no. 1, pp. 16–22, Jan. 2013, doi: 10.1111/j.1530-0277.2012.01869.x.

[25] “Layers of dermis - Labster Theory.” Accessed: Apr. 10, 2023. [Online]. Available: https://theory.labster.com/dermis_layers/

[26] Q. Zeng *et al.*, “Skin Tissue Engineering,” in *Comprehensive Biomaterials*, Elsevier, 2011, pp. 467–499. doi: 10.1016/B978-0-08-055294-1.00186-0.

[27] J. J. Lim, S. Grinstein, and Z. Roth, “Diversity and Versatility of Phagocytosis:

Roles in Innate Immunity, Tissue Remodeling, and Homeostasis," *Front. Cell. Infect. Microbiol.*, vol. 7, p. 191, May 2017, doi: 10.3389/fcimb.2017.00191.

[28] OpenStaxCollege, "Layers of the Skin," Mar. 2013, Accessed: Apr. 04, 2023. [Online]. Available: http://pressbooks-dev.oer.hawaii.edu/anatomyandphysiology/chapter/layers-of-the-skin/

[29] D. Yudovsky and L. Pilon, "Rapid and accurate estimation of blood saturation, melanin content, and epidermis thickness from spectral diffuse reflectance," *Appl. Opt.*, vol. 49, no. 10, p. 1707, Apr. 2010, doi: 10.1364/AO.49.001707.

[30] T. Igarashi, K. Nishino, and S. K. Nayar, "The Appearance of Human Skin: A Survey," *Found. Trends® Comput. Graph. Vis.*, vol. 3, no. 1, pp. 1–95, 2007, doi: 10.1561/0600000013.

[31] E. Hofmann, A. Schwarz, J. Fink, L.-P. Kamolz, and P. Kotzbeck, "Modelling the Complexity of Human Skin In Vitro," *Biomedicines*, vol. 11, no. 3, p. 794, Mar. 2023, doi: 10.3390/biomedicines11030794.

[32] U. Jung, J. Ryu, and H. Choi, "Optical Light Sources and Wavelengths within the Visible and Near-Infrared Range Using Photoacoustic Effects for Biomedical Applications," *Biosensors*, vol. 12, no. 12, p. 1154, Dec. 2022, doi: 10.3390/bios12121154.

[33] K. J. Zuzak, M. D. Schaeberle, M. T. Gladwin, R. O. Cannon, and I. W. Levin, "Noninvasive Determination of Spatially Resolved and Time-Resolved Tissue Perfusion in Humans During Nitric Oxide Inhibition and Inhalation by Use of a Visible-Reflectance Hyperspectral Imaging Technique," *Circulation*, vol. 104, no. 24, pp. 2905–2910, Dec. 2001, doi: 10.1161/hc4901.100525.

[34] R. L. Greenman *et al.*, "Early changes in the skin microcirculation and muscle metabolism of the diabetic foot," *The Lancet*, vol. 366, no. 9498, pp. 1711–1717, Nov. 2005, doi: 10.1016/S0140-6736(05)67696-9.

[35] D. A. Benaron *et al.*, "Design of a visible-light spectroscopy clinical tissue oximeter," *J. Biomed. Opt.*, vol. 10, no. 4, p. 044005, 2005, doi: 10.1117/1.1979504.

[36] L.-G. Lindberg, “Optical properties of blood in motion,” *Opt. Eng.*, vol. 32, no. 2, p. 253, 1993, doi: 10.1117/12.60688.

[37] M. Nitzan, I. Nitzan, and Y. Arieli, “The Various Oximetric Techniques Used for the Evaluation of Blood Oxygenation,” *Sensors*, vol. 20, no. 17, p. 4844, Aug. 2020, doi: 10.3390/s20174844.

[38] K. J. I. Ember *et al.*, “Raman spectroscopy and regenerative medicine: a review,” *Npj Regen. Med.*, vol. 2, no. 1, p. 12, May 2017, doi: 10.1038/s41536-017-0014-3.

[39] M. Shokrekhodaei and S. Quinones, “Review of Non-Invasive Glucose Sensing Techniques: Optical, Electrical and Breath Acetone,” *Sensors*, vol. 20, no. 5, p. 1251, Feb. 2020, doi: 10.3390/s20051251.

[40] “5.4: Infrared Spectroscopy,” Chemistry LibreTexts. Accessed: Jun. 09, 2023. [Online]. Available: https://chem.libretexts.org/Courses/Providence_College/Organic_Chemistry_I/05%3A_Analytical_Methods_for_Structure_Elucidation/5.04%3A_Infrared_Spectroscopy

[41] J. Jana, M. Ganguly, and T. Pal, “Enlightening surface plasmon resonance effect of metal nanoparticles for practical spectroscopic application,” *RSC Adv.*, vol. 6, no. 89, pp. 86174–86211, 2016, doi: 10.1039/C6RA14173K.

[42] L. Franzen and M. Windbergs, “Applications of Raman spectroscopy in skin research — From skin physiology and diagnosis up to risk assessment and dermal drug delivery,” *Adv. Drug Deliv. Rev.*, vol. 89, pp. 91–104, Jul. 2015, doi: 10.1016/j.addr.2015.04.002.

[43] R. Gillies, G. Zonios, R. Rox Anderson, and N. Kollias, “Fluorescence Excitation Spectroscopy Provides Information About Human Skin In Vivo,” *J. Invest. Dermatol.*, vol. 115, no. 4, pp. 704–707, Oct. 2000, doi: 10.1046/j.1523-1747.2000.00091.x.

[44] P. Liu, X. Mu, X.-D. Zhang, and D. Ming, “The Near-Infrared-II Fluorophores and Advanced Microscopy Technologies Development and Application in Bioimaging,” *Bioconjug. Chem.*, vol. 31, no. 2, pp. 260–275, Feb. 2020, doi:

10.1021/acs.bioconjchem.9b00610.

[45] V. V. Tuchin, “Light scattering study of tissues,” *Phys.-Uspekhi*, vol. 40, no. 5, pp. 495–515, May 1997, doi: 10.1070/PU1997v040n05ABEH000236.

[46] E. Austin *et al.*, “Visible light. Part I: Properties and cutaneous effects of visible light,” *J. Am. Acad. Dermatol.*, vol. 84, no. 5, pp. 1219–1231, May 2021, doi: 10.1016/j.jaad.2021.02.048.

[47] E. Hecht and A. Zajac, “Optics,” vol. 14, in Vol 3, vol. 14. , 2002, pp. 384–441.

[48] D. Tes *et al.*, “Granular Cell Tumor Imaging Using Optical Coherence Tomography,” *Biomed. Eng. Comput. Biol.*, vol. 9, p. 117959721879025, Jan. 2018, doi: 10.1177/1179597218790250.

[49] C. So-Ling and Ling Li, “A multi-layered reflection model of natural human skin,” in *Proceedings. Computer Graphics International 2001*, Hong Kong, China: IEEE Comput. Soc, 2001, pp. 249–256. doi: 10.1109/CGI.2001.934681.

[50] H. J. R. Dutton, *Understanding Optical Communications*. in ITSO networking series. Prentice Hall PTR, 1998. [Online]. Available: https://books.google.com.tr/books?id=iHCFQgAACAAJ

[51] W. J. Wadsworth *et al.*, “Very High Numerical Aperture Fibers,” *IEEE Photonics Technol. Lett.*, vol. 16, no. 3, pp. 843–845, Mar. 2004, doi: 10.1109/LPT.2004.823689.

[52] I. Oshina and J. Spigulis, “Beer–Lambert law for optical tissue diagnostics: current state of the art and the main limitations,” *J. Biomed. Opt.*, vol. 26, no. 10, Oct. 2021, doi: 10.1117/1.JBO.26.10.100901.

[53] H. Obrig and A. Villringer, “Beyond the Visible—Imaging the Human Brain with Light,” *J. Cereb. Blood Flow Metab.*, vol. 23, no. 1, pp. 1–18, Jan. 2003, doi: 10.1097/01.WCB.0000043472.45775.29.

[54] A. Huong, K. G. Tay, and X. Ngu, “Towards Skin Tissue Oxygen Monitoring: An Investigation of Optimal Visible Spectral Range and Minimal Spectral

Resolution," *Univers. J. Electr. Electron. Eng.*, vol. 6, no. 5B, pp. 49–54, Dec. 2019, doi: 10.13189/ujeee.2019.061607.

[55] P. E. Ong, A. K. C. Huong, X. T. I. Ngu, F. Mahmud, and S. P. Philimon, "Modified lambert beer for bilirubin concentration and blood oxygen saturation prediction," *Int. J. Adv. Intell. Inform.*, vol. 5, no. 2, p. 113, Jul. 2019, doi: 10.26555/ijain.v5i2.363.

[56] Y.-U. Ri, Y.-H. Pyon, H.-H. Ri, and K.-R. Sin, "Estimation of the hemoglobin concentration and the anatomic structure of muscle by analyzing the near infrared scattering images," *Biomed. Signal Process. Control*, vol. 61, p. 102058, Aug. 2020, doi: 10.1016/j.bspc.2020.102058.

[57] S. L. Jacques, "Corrigendum: Optical properties of biological tissues: a review," *Phys. Med. Biol.*, vol. 58, no. 14, pp. 5007–5008, Jul. 2013, doi: 10.1088/0031-9155/58/14/5007.

[58] S. Pissadakis, "Laser processing of optical fibers: new photosensitivity findings, refractive index engineering and surface structuring," in *Laser Growth and Processing of Photonic Devices*, Elsevier, 2012, pp. 374–452. doi: 10.1533/9780857096227.3.374.

[59] T. Lister, P. A. Wright, and P. H. Chappell, "Optical properties of human skin," *J. Biomed. Opt.*, vol. 17, no. 9, p. 0909011, Sep. 2012, doi: 10.1117/1.JBO.17.9.090901.

[60] M. Drahanský, O. Kanich, E. Brezinová, and K. Shinoda, "Experiments with Optical Properties of Skin on Fingers," 2016. Accessed: Apr. 10, 2023. [Online]. Available: https://www.semanticscholar.org/paper/Experiments-with-Optical-Properties-of-Skin-on-Drahansk%C3%BD-Kanich/a3c46a7abb589a4f7030c2115370aa8b61d10f66

[61] S. Jacques, "Origins of tissue optical properties in the UVA, visible, and NIR regions," *Adv Opt Imaging Photon Migr.*, vol. 2, Jan. 1996.

[62] Y. Pu, J. Chen, W. Wang, and R. R. Alfano, "Basic Optical Scattering Parameter of the Brain and Prostate Tissues in the Spectral Range of 400–2400 nm,"

in *Neurophotonics and Biomedical Spectroscopy*, Elsevier, 2019, pp. 229–252. doi: 10.1016/B978-0-323-48067-3.00011-1.

[63] Y. A. Eremin, "SCATTERING | Scattering Theory," in *Encyclopedia of Modern Optics*, Elsevier, 2005, pp. 326–330. doi: 10.1016/B0-12-369395-0/00682-5.

[64] S. Jacques, C. A. Alter, and S. Prahl, "Angular Dependence of HeNe Laser Light Scattering by Human Dermis," *Lasers Life Sci.*, vol. 1, pp. 309–333, Jan. 1987.

[65] D. Toublanc, "Henyey–Greenstein and Mie phase functions in Monte Carlo radiative transfer computations," *Appl. Opt.*, vol. 35, no. 18, p. 3270, Jun. 1996, doi: 10.1364/AO.35.003270.

[66] L. Wang, S. L. Jacques, and L. Zheng, "MCML—Monte Carlo modeling of light transport in multi-layered tissues," *Comput. Methods Programs Biomed.*, vol. 47, no. 2, pp. 131–146, Jul. 1995, doi: 10.1016/0169-2607(95)01640-F.

[67] J. Jiang, W. Chen, L. Zhang, R. K. Wang, and K. Xu, "Monte Carlo simulation on how optical clearing technique influences predicting precision of non-invasive optical blood glucose sensing," presented at the SPIE BiOS, San Francisco, California, USA, Feb. 2011, p. 789810. doi: 10.1117/12.874028.

[68] A. Barbu and S.-C. Zhu, *Monte Carlo Methods*. Singapore: Springer Singapore, 2020. doi: 10.1007/978-981-13-2971-5.

[69] S. S. Qian, C. A. Stow, and M. E. Borsuk, "On Monte Carlo methods for Bayesian inference," *Ecol. Model.*, vol. 159, no. 2–3, pp. 269–277, Jan. 2003, doi: 10.1016/S0304-3800(02)00299-5.

[70] M. Born and E. Wolf, *Principles of optics: electromagnetic theory of propagation, interference and diffraction of light*, 6th ed. Oxford ; New York: Pergamon Press, 1980.

[71] C.-P. Chang, P.-C. Tung, L.-H. Shyu, Y.-C. Wang, and E. Manske, "Fabry–Perot displacement interferometer for the measuring range up to 100 mm," *Measurement*, vol. 46, no. 10, pp. 4094–4099, Dec. 2013, doi: 10.1016/j.measurement.2013.06.029.

[72] J. Sandby-Møller, T. Poulsen, and H. C. Wulf, “Epidermal Thickness at Different Body Sites: Relationship to Age, Gender, Pigmentation, Blood Content, Skin Type and Smoking Habits,” *Acta Derm. Venereol.*, vol. 83, no. 6, pp. 410–413, Nov. 2003, doi: 10.1080/00015550310015419.

[73] N. Ren, J. Liang, X. Qu, J. Li, B. Lu, and J. Tian, “GPU-based Monte Carlo simulation for light propagation in complex heterogeneous tissues,” *Opt. Express*, vol. 18, no. 7, p. 6811, Mar. 2010, doi: 10.1364/OE.18.006811.

[74] S. Ren *et al.*, “Molecular Optical Simulation Environment (MOSE): A Platform for the Simulation of Light Propagation in Turbid Media,” *PLoS ONE*, vol. 8, no. 4, p. e61304, Apr. 2013, doi: 10.1371/journal.pone.0061304.

[75] B. Nasouri, T. E. Murphy, and H. Berberoglu, “Simulation of laser propagation through a three-layer human skin model in the spectral range from 1000 to 1900 nm,” *J. Biomed. Opt.*, vol. 19, no. 7, p. 075003, Jul. 2014, doi: 10.1117/1.JBO.19.7.075003.

[76] A. N. Bashkatov, E. A. Genina, and V. V. Tuchin, “OPTICAL PROPERTIES OF SKIN, SUBCUTANEOUS, AND MUSCLE TISSUES: A REVIEW,” *J. Innov. Opt. Health Sci.*, vol. 04, no. 01, pp. 9–38, Jan. 2011, doi: 10.1142/S1793545811001319.

[77] A. N. Bashkatov, E. A. Genina, V. I. Kochubey, V. S. Rubtsov, E. A. Kolesnikova, and V. V. Tuchin, “Optical properties of human colon tissues in the 350 – 2500 nm spectral range,” *Quantum Electron.*, vol. 44, no. 8, pp. 779–784, Aug. 2014, doi: 10.1070/QE2014v044n08ABEH015613.

[78] M. Mamouei, S. Chatterjee, M. Razban, M. Qassem, and P. A. Kyriacou, “Design and Analysis of a Continuous and Non-Invasive Multi-Wavelength Optical Sensor for Measurement of Dermal Water Content,” *Sensors*, vol. 21, no. 6, p. 2162, Mar. 2021, doi: 10.3390/s21062162.

[79] R. H. Wilson, K. P. Nadeau, F. B. Jaworski, B. J. Tromberg, and A. J. Durkin, “Review of short-wave infrared spectroscopy and imaging methods for biological tissue characterization,” *J. Biomed. Opt.*, vol. 20, no. 3, p. 030901, Mar. 2015, doi: 10.1117/1.JBO.20.3.030901.

[80] A. Roggan, M. Friebel, K. Dörschel, A. Hahn, and G. Müller, “Optical Properties of Circulating Human Blood in the Wavelength Range 400–2500 nm,” *J. Biomed. Opt.*, vol. 4, no. 1, p. 36, 1999, doi: 10.1117/1.429919.

[81] C. C. Cooksey and D. W. Allen, “Reflectance measurements of human skin from the ultraviolet to the shortwave infrared (250 nm to 2500 nm),” presented at the SPIE Defense, Security, and Sensing, G. C. Gilbreath and C. T. Hawley, Eds., Baltimore, Maryland, USA, May 2013, p. 87340N. doi: 10.1117/12.2015821.

[82] C. C. Cooksey, B. K. Tsai, and D. W. Allen, “Spectral reflectance variability of skin and attributing factors,” presented at the SPIE Defense + Security, K. I. Ranney, A. Doerry, G. C. Gilbreath, and C. T. Hawley, Eds., Baltimore, Maryland, United States, May 2015, p. 94611M. doi: 10.1117/12.2184485.

[83] S. Chatterjee, K. Budidha, M. Qassem, and P. A. Kyriacou, “In-silico investigation towards the non-invasive optical detection of blood lactate,” *Sci. Rep.*, vol. 11, no. 1, p. 14274, Jul. 2021, doi: 10.1038/s41598-021-92803-x.

[84] J. A. Carr, M. Aellen, D. Franke, P. T. C. So, O. T. Bruns, and M. G. Bawendi, “Absorption by water increases fluorescence image contrast of biological tissue in the shortwave infrared,” *Proc. Natl. Acad. Sci.*, vol. 115, no. 37, pp. 9080–9085, Sep. 2018, doi: 10.1073/pnas.1803210115.

[85] A. Roggan, J. Beuthan, S. Schrunder, and G. Mueller, *Diagnostik und Therapie mit dem Laser*. 1999.